10-24-2018

Hyperspectral Imaging for Characterizing Single Plasmonic Nanostructure and Single-Cell Analysis

Nishir Sanatkumar Mehta
Louisiana State University and Agricultural and Mechanical College

HYPERSPECTRAL IMAGING FOR CHARACTERIZING SINGLE PLASMONIC NANOSTRUCTURE AND SINGLE-CELL ANALYSIS

A Thesis

Submitted to the Graduate Faculty of the
Louisiana State University and
Agricultural and Mechanical College
In partial fulfillment of the
Requirements for the degree of
Master of Science

in

The Department of Mechanical Engineering

by

Nishir Sanatkumar Mehta
B.Tech, Narsee Monjee Institute of Management Studies, 2015
December 2018

Acknowledgements

I would sincerely like to thank my adviser Dr. Manas Ranjan Gartia for his invaluable motivation, guidance, and support throughout my master's research. I would like to express my gratitude to Dr. Ram Devireddy, Shahensha Shaik, and Rachel at LSU Bioengineering Lab; to Dr. Dongmei Cao and Dr. Clayton Loehn at Shared Instrumentation Facility; to Dr. Varshini Singh at Center for Advanced Microstructures and Devices (CAMD); to Dr. Kevin McPeak and Tiago Ramos at LSU Chemical Engineering; to Dr. Georgios Veronis and Amirreza Mahigir at School of Electrical Engineering; and to Elyse Johnson at CytoViva.

I would like to acknowledge my committee members Dr. Sunggook Park and Dr. Ram Devireddy for agreeing to be in my committee; and for their support and advices. I would personally like to thank my lab mates Abid, Steven, Ardalan, and Alisha for their continuous assistance.

I would like to thank my parents, my sister and brother-in-law, extended family, beloved one, and little niece for their encouragement, love and support which has been vital for completing this research.

The research reported here was supported, in part, by the Louisiana Board of Regents through the Board of Regents Support Fund (Contract Number: LEQSF (2017-20)-RD-A-04 and LEQSF (2017-18)-ENH-TR-08) and National Science Foundation (Award Number: 1660233). Dr. Manas Gartia thanks Louisiana State University start-up funds for partially supporting the research.

This thesis features my first authored work that originally appeared in:

1) Single-Cell Analysis Using Hyperspectral Imaging Modalities,

Citation: Mehta N, Shaik S, Devireddy R, Gartia M. Single-Cell Analysis Using Hyperspectral Imaging Modalities. ASME. J Biomech Eng. 2018; 140(2):020802-020802-16. doi:10.1115/1.4038638.

Reprinted with permission from ASME Journal of Biomechanical Engineering. All authors contributed to writing this manuscript.

2) Orientational imaging of a single plasmonic nanoparticle using dark-field hyperspectral imaging,

Citation: Nishir Mehta, Amirreza Mahigir, Georgios Veronis, Manas Ranjan Gartia, "Orientational imaging of a single plasmonic nanoparticle using dark-field hyperspectral imaging," Proc. SPIE 10346, Plasmonics: Design, Materials, Fabrication, Characterization, and Applications XV, 1034631 (25 August 2017); doi: 10.1117/12.2274695; https://doi.org/10.1117/12.2274695.

Reprinted with permission from SPIE Digital Library. All authors contributed to writing this manuscript.

TABLE OF CONTENTS

Abstract

Orientation of plasmonic nanostructures is an important feature in many nanoscale applications such as photovoltaics, catalyst, biosensors DNA interactions, protein detections, hotspot of surface-enhanced Raman spectroscopy (SERS), and fluorescence resonant energy transfer (FRET) experiments. Silver nanocubes with significant spectral signatures between 400-700 nm are observed in this experimental research. Whereas study of single cells will enable the analysis of cell-to-cell variations within a heterogeneous population. These variations are important for further analysis and understanding of disease propagation, drug development, stem cell differentiation, embryos development, and how cells respond to each other and their environment. Adipose-derived mesenchymal stem cells possess the capability to undergo differentiation into adipocytes, chondrocytes, and adipocytes and convert to adipose tissues, bones, and cartilages respectively. This regenerative ability has augmented stem-cell research and the need to characterize them quickly with minimal invasiveness. An imaging and spectroscopic technology supported with correlative techniques which can address the capability to probe single stem-cell and single nanostructure non-invasively, without photo bleaching, is accurate, quick, cost-efficient, requires simple sample preparation, and curbs diffraction limitations are implemented in this research.

Almost a decade ago, Hyperspectral Imaging (HSI) was employed by the NASA in satellite imaging applications such as remote sensing technology. This technology has since been extensively used in the exploration of minerals, agricultural purposes, water resources, and urban development needs. Due to recent advancements in optical re-construction, imaging, and advance computing technologies, HSI can now be applied down to micro- and nano-meter scales possibly allowing for exquisite control and quantitative spectral analysis of single nanostructures to ensemble spectroscopy and single cell to complex biological systems.

In this work, we use transmitted dark field imaging technique to locate individual nanostructure and single stem-cell on a glass substrate. Then we employ a hyperspectral imaging technique within Vis-NIR spectrum (400-900 nm) at the same spot to collect spectral response of a single silver nanoparticle and single ASCs. No special tagging or staining of the nanoparticle or biological cell has been done, as more likely required in traditional microscopy techniques. Different orientations exhibiting dissimilar dipole moments and differentiated stem-cells with variable tissue scattering have been identified by carefully understanding and analyzing shift in spectral response from the sample.

The orientations measured by hyperspectral microscopy were validated using the finite difference time domain (FDTD) electrodynamics calculations and correlative scanning electron microscopy (SEM) analysis. The combination of high resolution nanometer-scale imaging techniques and the modern numerical modeling capacities thus enables a meaningful advance in our knowledge of manipulating plasmon response and fabricating shaped nanostructures. To obtain insight of single molecule-level proteins, fats, and other constituents, matrix-assisted laser deposition/ionization (MALDI) was performed on stem-cells. Spectra collected from these mono-constituents were required to create libraries. Using the library data, then cells were mapped via single angle mapping (SAM) algorithms. The optical images were characterized using template match and edge detection algorithms to analyze the cell differentiation. Developing this label-free protocol enables the possibility to non-invasively analyze stem cell differentiation.

This work has advanced our understanding of the behavior of small nanoparticle clusters and single stem cell probing protocol useful for sensing, nanomedicine, tissue regeneration, cellular morphological analysis, and surface sciences.

CHAPTER 1: INTRODUCTION

1.1. Motivation

Nanotechnology applications are becoming omnipresent in a variety of daily activities and research endeavors. For example, investigating, fabricating, and modifying substances at the nanoscale has helped advance and transform products ranging from clothing/wearable technologies, bio-sensors, coatings with self-healing capacities, energy storage and transmission, sports equipment to computers. Concurrently, significant improvements in the field of nano-imaging and analysis have vastly improved the modalities in precision/personalized medicine, photovoltaics, energy enhancement, targeted drug delivery systems and image-guided surgery. To further advance these transformative activities precise and highly accurate probing methods to detect, characterize, and measure distinct characteristics of nano-substances are required, apart from the currently available microscopy and spectroscopy technologies such as optical microscopy [1, 2], transmission electron microscopy [3, 4] and electron energy-loss spectroscopy, cryo-electron-microscopy [5, 6], atomic force microscopy [7, 8], scanning ion-conductance microscopy, atom probe tomography [9, 10], positron emission tomography [11, 12], scanning electro-chemical microscopy [13], X-ray microscopy [14, 15], linear & nonlinear vibrational spectroscopy [16, 17], mass spectrometry, Fourier-transformed infrared (FTIR) spectroscopy, photo thermal imaging [18], and nuclear magnetic resonance imaging with paramagnetic metal particles [19, 20]. Microscopy technologies provide two-dimensional intensity information at each pixel (x, y) of the images. On the other hand, spectroscopy technologies provide averaged spectral information (λ) of the entire field of view. Hyperspectral imaging (HSI) combines both of these modalities by providing intensity and spectral information (x, y, λ) at each pixel. These new techniques can be either used for preliminary survey/validation tool or replace traditional methods [21].

1.2. Principle

When electromagnetic radiation is incident on the sub-wavelength level nano-sized particles, there is a formation of approximated dipole moment amongst free electrons cloud on the dielectric materials. At the optical cross-section, incoming photons are either scattered or absorbed creating resonance of the dipoles and generating strong optical response from the nano-particles. When a precisely deflected beam of light enters or impinges upon a heterogeneous sample (for example, a surface or a biological tissue or cell), various light-matter interactions such as scattering, absorption, and transmission takes place due to the intrinsic radiative properties of the surface and/or the sample. These radiative properties can be correlated to, and are intrinsic, to the multiple multi-sized structures and/or organelles present within the sample.

The underlying principle of spectral imaging (e.g. HSI), thus, is simple and straightforward: By quantifying the radiative properties (reflectance or absorbance in-homogeneities) for a given sample at the sub-wavelength level, it should be possible to analyze and assess characteristics of the system under investigation. Spectral imaging is typically achieved by a combination of optical imaging with specialized spectrographic attachments for data storage as well as specialized software for data analysis [22]. Due to successive advancements in optical simulation techniques and optics, spectral imaging can now be translated down to macro- and nano-scales and radiative properties collected across the entire electromagnetic spectrum; such a system is termed as hyper spectral imaging (HSI). Specifically, advances in dark-field imaging conditions enabled high contrast and signal-to-noise ratio and consequently, an ability to focus light on samples with high collimation even at oblique angles and with controlled detection settings [23-25]. HSI enables precise information (quantitative and qualitative) about various surfaces and morphologies to be stored in the form of optical images. These optical images consist of hundreds of pixels; each pixel

is stored as a three-dimensional hypercube data-set containing information on two spectral dimensions and one spatial dimension [26, 27]. Ideally, the hypercube data from the entire electro-magnetic spectrum in visible-near infrared range is stored using an imaging spectrophotometer. The stored data can then be compared and cross-correlated with previously obtained reference spectral libraries to develop protocols for precise and quick analysis of micro- and nano-materials. Additionally, by integrating HSI with other imaging techniques one can produce complimentary data; for example, in combination with fluorescence microscopy one can also obtain information about chemical changes or by solely using light for quantification without any additional probes, one can develop noninvasive medical diagnostic platforms as well as image guided surgical techniques [26].

1.3. Outline

This thesis is organized in different chapters. Chapter 1 provides introduction of the thesis. Chapter 2 provides an overview of hyperspectral imaging system. Chapter 3 shows the orientational imaging of single plasmonic nanoparticle. Chapter 4 demonstrates noninvasive analysis of single stem-cell differentiation. Chapter 5 provides the summary and future work for the thesis. Finally, Chapter 6 identifies the limitation of the method mentioned in the thesis. The chapters are outlined to provide research findings on detecting orientation of single nano-particles using hyperspectral dark-field imaging and developing non-invasive method to detect stem-cell differentiation using HSI along with information on nanoscale plasmonics and information on biological optics. Overview on hardware and software of the system is also mentioned in the thesis (Chapter 2) in order to understand the system before diving into the details of the experimental procedure for each experiment.

CHAPTER 2: OVERVIEW OF HYPERSPECTRAL IMAGING SYSTEM

Traditionally, the following spectral ranges have been defined for various imaging techniques: ultraviolet (200 to 400 nm), visible (400 to 780 nm), near-infrared (780 to 2,500 nm) and mid-infrared (2,500 to 25,000 nm) as shown in Figure 1. The imaging modalities are generally categorized into: monochrome, RGB, spectroscopy, multispectral, and hyperspectral imaging.

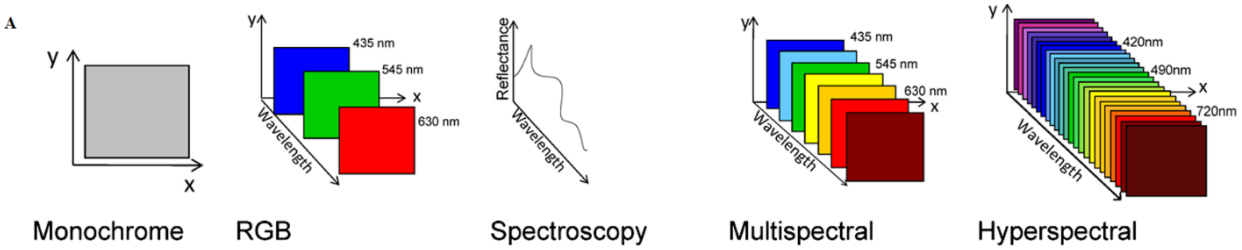

Figure 1: Schematic showing the differences between monochrome, RGB, spectroscopy, multispectral, and hyperspectral imaging [26]

Appendix-A provides information on differences between HSI and RGB as well as information on various types of hyperspectral imaging systems available in the market.

Additionally, HSI unlike other spectral imaging methods, collects and processes information from across the entire electromagnetic spectrum [22-25, 28]. Figure-2 shows complete schematic diagram of a typical optical path within HIS system.

The various hardware components of a typical HSI system are as follows:

i) a light source to illuminate the sample and depending on the application, is either a light emitting diode or a halogen bulb or a tunable laser. The source image is eliminated by passing the light through light-guide and the image is further reflected inside a light adapter.

ii) a high resolution light collimator or adapter.

iii) A visible and hyperspectral spectrometer or detector array which is situated at the focal point in the HSI setup and receives and converts the electromagnetic energy into electrical signals for

hyperspectral image formation. Charged-coupled devices (CCDs) are widely used as detector arrays and are mainly made up of materials like silicon, indium gallium arsenide, mercury cadmium telluride, and indium antimonite. A cooling system is typically attached to the CCDs to reduce thermal vibrations and to minimize dark-current noises. Other detector arrays used in HSI systems are photomultiplier tubes and metal oxides [26].

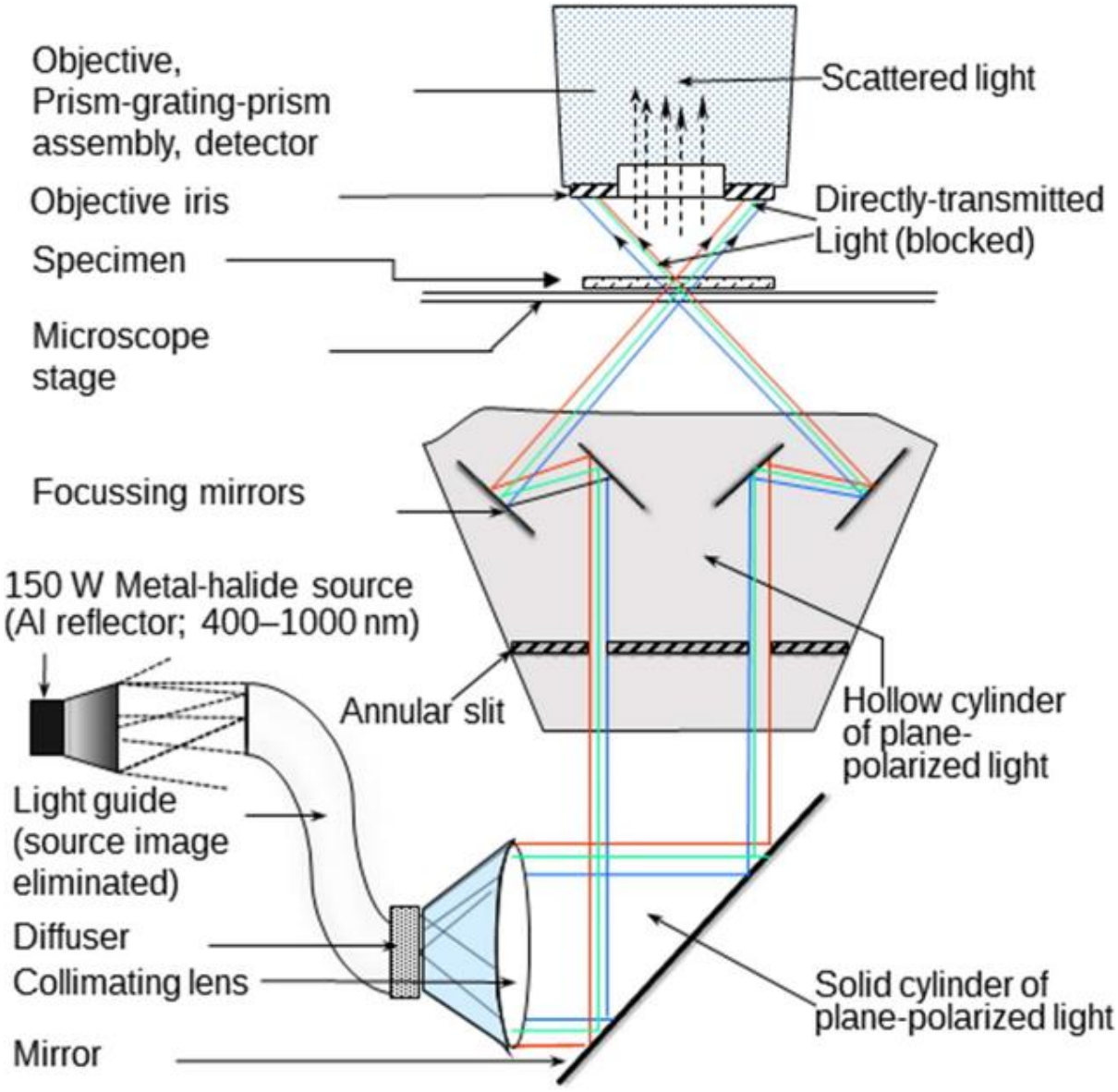

Figure 2: Condenser optics of CytoViva hyperspectral imaging system [25, 29]

iv) a stage that commonly includes an optical microscope or a Fourier transform spectrometer and/or a Raman imaging system.

v) an optical dual mode fluorescence module coupled with an optical imaging camera and other lens/slit combinations for bright-field and dark-field analysis.

vi) several light dispersive elements such as prism-grating, monochromatic lens or optical filters. These elements disperse incident white light into its constituent color spectrum and project the spectrum onto the detector arrays. Grating based spectrograph is shown in Figure-3.

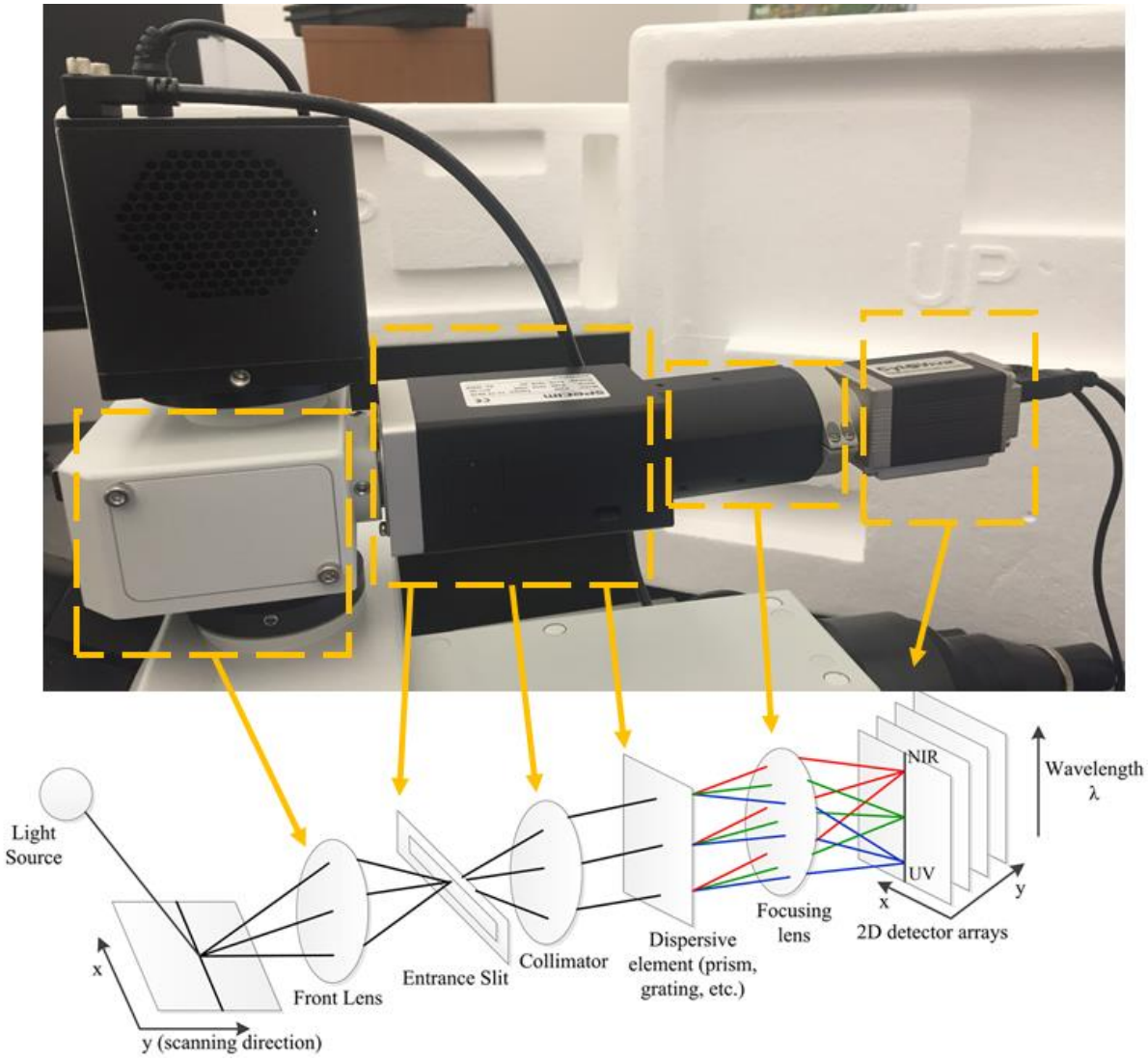

Figure 3: Hyperspectral imaging system spectrograph light path and optics [26, 29]

vii) Different HSI image capture schemes are implemented in commercial microscopy systems. These HSI image capture schemes are classified as whiskbroom (spatial or point scan), pushbroom (line scanning), staring (spectral scan) and snapshot (no scan). All these hyperspectral data cube acquisition strategies affect the light throughput and image acquisition time. For example, the snapshot will be the fastest one as it captures the whole data cube in a single acquisition.

viii) Software for the hyperspectral imaging system is highly specialized. For example, the number of scan lines and the RGB default bands are user defined in accordance with the desired field of view and the sensitivity of the application. In general, 200-300 lines are sufficient for single cell imaging. Proprietary imaging software provides an easy to use interface to enhance acquired images and to improve the signal-to-noise ratio by filtering end wavelengths. Spectral data of each pixel or for a collection of selected area pixels as well as that of an entire image can be stored in the spectral library for further analysis. Ideally, the imaging software should also provide a normalizing procedure to filter out spectral irregularities, loss of information, and to account for false information due to effects of fiber optics cables, camera, and the spectrograph. The most important function embedded within the imaging software is the SAM or spectral angle mapping function. As described in the CytoViva system user manual, the SAM method determines the distance from the origin to the intensity of light registered in each band of the known spectrum (such as control or reference sample) and the unknown spectrum (target sample under probe) and stores this as an N-dimensional vector(s). The direction of these vector(s) is a unit vector in the N-dimensional space representing the unknown as well as the reference spectrum. The angle between these two unit vectors one obtained from the sample and another from the reference is a measure of spectral match or mismatch between them. Thus, by analyzing the data cube and comparing the spectrum at each pixel from different samples one can deduce similarities and differences between

samples and subsequently, if baseline (reference) libraries are available, precise and quantitative analysis of the samples can also be performed with the purpose of finding objects, identifying materials, or detecting processes.

In Table A.1 of Appendix-A, information regarding various different commercially available hyperspectral imaging systems is provided.

CHAPTER 3: ORIENTATIONAL IMAGING OF SINGLE PLASMONIC NANOPARTICLE

3.1. Literature Review and Theory

Existing methods of interrogation of nanoparticles like fluorescence polarization spectroscopy are not feasible to obtain single particle level information on a large scale (to have statistical significance of the results), are time intensive, expensive and require many resources for sample preparation and analysis [30]; in addition the conventional optical microscope is diffraction limited (~ 250 nm) and only provides intensity images without spectral information. Fluorescence dye labelled nanoparticles are prone to photo-bleaching and the intensity is distance dependent (how far the dye is located from the nanoparticle surfaces). Conventional techniques to characterize nanoparticles such as fluorescence imaging and magnetic resonance spectroscopy [31] involve complex sample preparation, probing and labelling expertise. When nano structures are characterized using ensemble methods, many of the properties are heterogeneously lost or hidden as well as predicted on much broader sense. Hence ability to get information from one single particle at a time can solve this issue. Therefore, new probing methods such as hyperspectral imaging system are needed to investigate characteristics of nanoscale structures that can be done in a label-free and efficient manner on large scale.

Localized surface plasmon resonance is generated when there is collective electron oscillation triggered by incident electromagnetic radiation as shown in Figure-4. Plasmon response from the nanostructures can be tuned ranging from ultraviolet spectrum to visible region to near-infrared spectrum in the electromagnetic spectral range. This change in optical response can be achieved by modifying/changing size of the particles, shape and material composition. By controlling the dimension for individual nano-structures, we can modify the color of dispersions and thin films.

Most recurring used metal particles are made of gold, silver or platinum. Phenomenon termed as 'Surface Plasmon Resonance' is created due to relative oscillation of electrons on the metal nanostructures. The harmonious oscillation of the electrons in nano-particles is created because only certain wavelengths from the entire electromagnetic spectrum are absorbed and scattered by the nanoparticles. All the radiation which are incident on these nano-structures eventually become extinct and the phenomena is described as extinction spectrum. These absorbed wavelengths from illumination source interact with surface electron cloud to excite the absorption and scattering intensities almost 50 times than nano-particles which are non-plasmonic in nature [32].

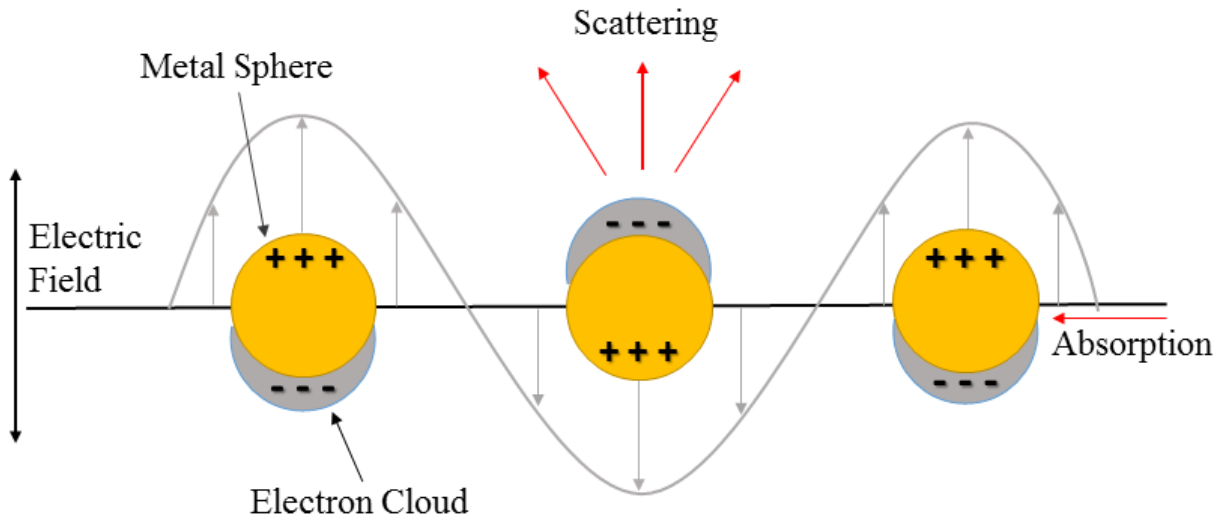

Figure 4: Optical cross-section depicting extinction (scattering and absorbance) when electromagnetic radiation is incident on the nanostructures

Optical properties of metal nano-particles are significantly dominated by surface plasmon (oscillation of electrons). Energies stored in visible and mid-infrared region of light spectrum are enough to excite the surface plasmons of nanostructures because these energies correspond to the atomic transitions and molecular vibrations [33]. The plasmon resonance characteristics of the nano-particles which have dielectric constant with small imaginary part and negative real part depend mainly on particle size, material, shape and orientation, especially when the structures are

small compared to incident wavelength of light [34]. Optical response due to surface plasmons is dominated by the orientation of the nanostructures while probing the structures with similar size and shape. Red shifting or blue shifting in scattering spectra of nano-particles are observed due to the difference in the excitation frequency-dependent plasmons wave-vector that are directly corresponding to the different orientations of these nano-particles. By controlling the plasmon excitation and emission with orientation of nano-particles, there is a possibility of condensing and channeling light at subwavelength level [35].

Principles of conventional geometrical optics and ray trace method is used when the diameter of the object under investigation is greater than the wavelength of incident light. Intensity distribution of the interference and diffraction patterns are studied to characterize the subjects whose dimensions are equivalent to the wavelength of the incident light i.e. x-ray. In this research, focus is only channeled to evaluate properties of the objects whose radius is much smaller than the wavelength of the incident light. Due to a (radius) << λ, we can assume quasi-static condition and directly apply harmonic wave equation model to provide analytical solution to Maxwell's equations. Materials that have small positive part of the dielectric constant and negative real part generally exhibit surface plasmon resonance properties. Mie theory can provide theoretical values of the optical response by providing analytical solution to Maxwell's equations. Considering quasi-static condition, electric field around the nano-structures is considered constant and theoretical solutions can be provided by accounting spherical wave harmonics [36, 37].

Mie theory polarizability equation is true for particles spherical in nature. This equation does not hold true for more complicated geometries. Generalized steps of derivation [38] are provided in Appendix-B. While Rayleigh-Gans theory can provide theoretical solution for ellipsoidal nano-particles [38].

$$S_{Scattering} = \frac{24\,\pi^3 V^2 \epsilon_n^2}{\lambda_o^4} \frac{(\epsilon_{real} - \epsilon_n)^2 + \epsilon_{img}^2}{(\epsilon_{real} + 2\epsilon_n)^2 + \epsilon_{img}^2}$$

$$\text{Here we consider } l = 1 \text{ (dipole)}$$

$$S_{absorbance} = \frac{18\,\pi V \epsilon_n^{\frac{3}{2}}}{\lambda_o} \frac{\epsilon_{img}^2}{(\epsilon_{real} + 2\epsilon_n)^2 + \epsilon_{img}^2}$$

Rayleigh-Gans theory provides analytical solutions for scattering and absorbance spectrum for ellipsoidal nano-structures.

$$S_{Scattering} = \frac{8\,\pi^3 V^2 \epsilon_n^2}{9\lambda_o^4} \sum_{p=1}^{3} \frac{1}{I_p^2} \frac{(\epsilon_{real} - \epsilon_n)^2 + \epsilon_{img}^2}{(\epsilon_{real} + \frac{(1 - I_p)}{I_p}\epsilon_n)^2 + \epsilon_{img}^2}$$

$$S_{absorbance} = \frac{2\pi V \epsilon_n^{\frac{3}{2}}}{3\lambda_o} \sum_{p=1}^{3} 1 \frac{\epsilon_{img}\,(\frac{1}{I_p^2})}{(\epsilon_{real} + \frac{(1 - I_p)}{I_p}\epsilon_n)^2 + \epsilon_{img}^2}$$

$$\text{Here, } V = \text{volume, } \epsilon_n = \text{dieletric permittivity of surrounding,}$$

$$\epsilon_{real} \text{ and } \epsilon_{img} = \text{real and imaginary components of permittivity of metal}$$

$$\lambda_o = \text{wavelength of the incident light and } I_p = \text{depolarization factors}$$

In the above equation, we can note that as the volume increases, scattering from the particle becomes more dominant than the absorption. Therefore it is noted from the theoretical calculations that for particle sizes above 20 nm, scattering is more dominant than absorption in the overall extinction spectrum as shown in Figure-5 by plotting Mie equations with varying radius of nanostructure from 0 to >60nm. And resonance is achieved at E (real) =-2 E (medium). Dielectric function can be modified in a broader sense by accounting for nonlocal effects, electron spill out, strong damping due to extremely small size of the particles. The case when the electrons will not have enough mean free path to move within the electron cloud. In such cases, there is strong

electron-scattering and hence large damping effect. There is the dissipation of electric field when charges are in motion. Hence imaginary component of the relative dielectric permittivity takes into consideration this phenomena.

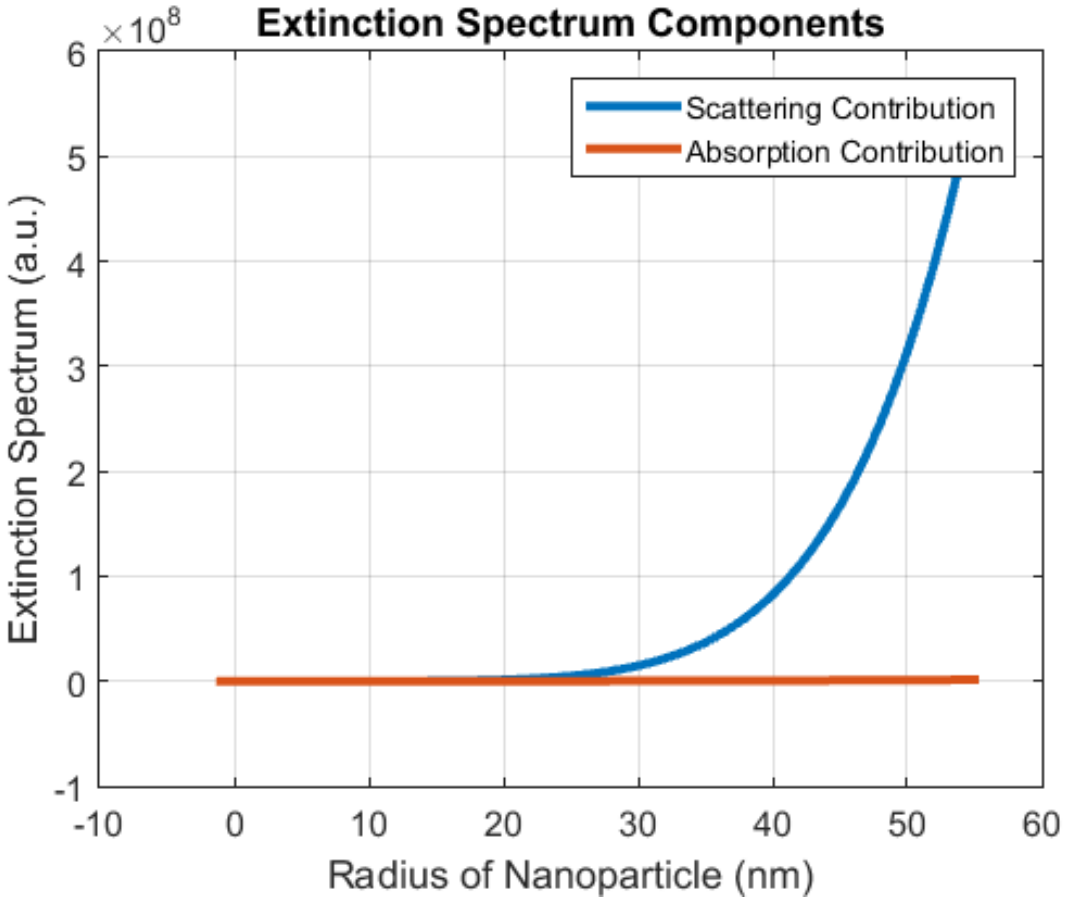

Figure 5: Extinction spectra components (scattering, absorption) as given by Mie-theory are plotted as a function of radius of the nanostructure

Dielectric environment around the nanostructures and the geometrical properties have significant impact on the spectral response exhibited by these particles. Unique property is that nanoparticles scatter and absorb light at specific wavelengths. The exhibited color of the nanostructures illuminated by incident electromagnetic radiation is mainly dependent on material of metal, shape and size of individual structures as shown in Figure-6. Size and shape distribution can be achieved with good consistency due to modern chemical engineering process techniques.

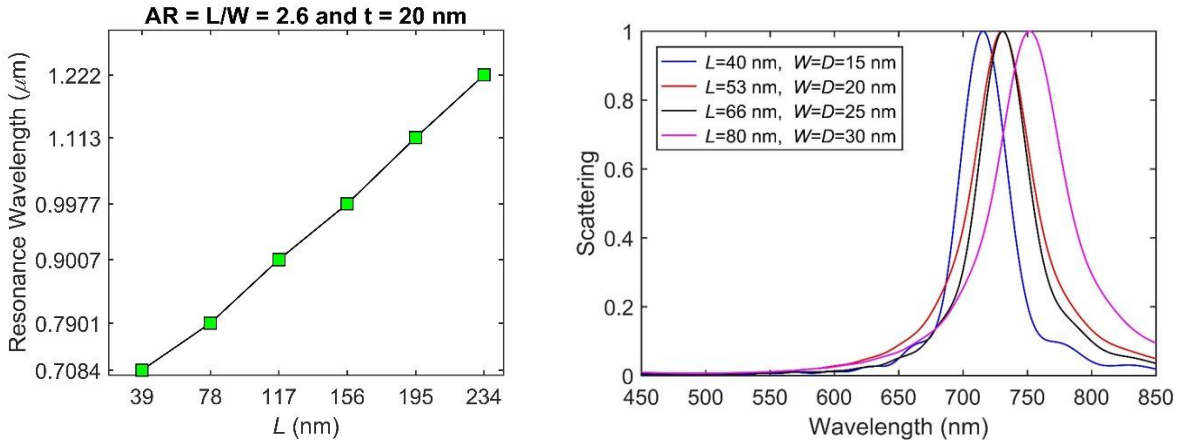

Figure 6: Representation of size-dependence of resonance wavelength of nano-particles. Red-shift in resonance is observed with increase in length (fixed aspect ratio and thickness) and increasing dimensions

Metallic nanostructures have very different mechanical, electric, and optical properties compared to macro/micro metal particles. These particles exhibit variety of colors and hence can be used for engineering application which can be color-defined such as plasmonic sensors for medical diagnosis, cancer detection, targeted drug delivery, manufactured composite materials, anti-microbe coatings, ceramics, photovoltaics, surface enhanced Raman spectroscopy, and more. Pictorial representation of some of the applications is shown in Figure-7.

What we attempted to probe in this experiment is dependency of nanostructure plasmonics based on orientation of individual structures. Information about the orientation of plasmonic nanostructures is highly important for the study of biomolecular absorption and developing bio-optical sensing platform, protein-protein interaction, drug-protein detections, and opto-magnetic data storing devices. Control over orientation is important in order to modify single-nanoparticle to create Janus particles as well as to create dimers by placing two different metal nanostructures in close vicinity [39]. By developing this non-invasive probing protocol, we also develop ground for scattering based probing of more heterogeneous and complex nano-structures. This method can also be applied to in vivo studies of interaction of nanoparticles with biological cells that can provide intracellular information.

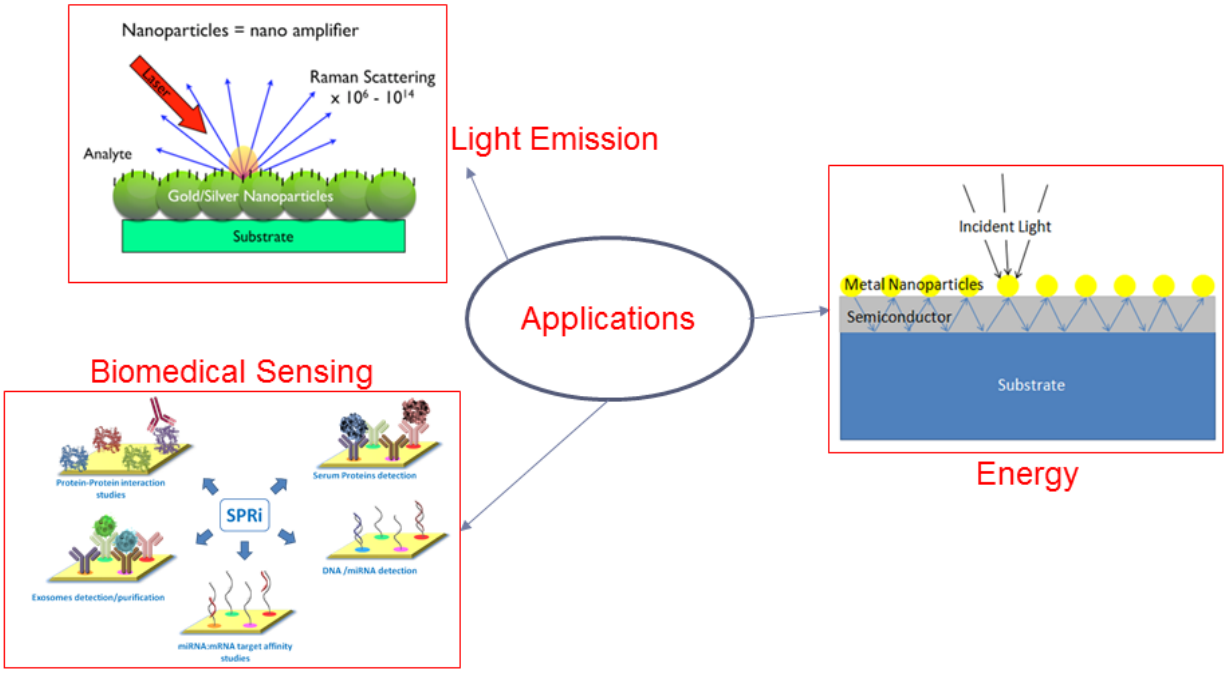

Figure 7: Applications of nano-particles in energy, bio sensing, and light emission [40-42]

Chang et al in "Plasmonic Nano rod absorbers as orientation sensors" utilized absorption based spectroscopy such as photo thermal imaging to detect orientation of Au Nano rods (25 X 73 nm) [43]. According to analytical solutions of Gans theory and Mie theory in the aforementioned mathematical relationships, nanostructures above 20 nm have scattering field as major contributor to extinction. Hence scattering based technique to detect orientation is important. Tablor et al in "Effect of Orientation on Plasmonic Coupling between Gold Nano rods" have applied grid-based discrete dipole approximation (DDA) to establish mathematical relationship between effects of orientation on spectral shift [44]. Many studies have been pursued to find effect of size, shape, dielectric environment on metal nanostructures. For example, "The Optical Properties of Metal Nanoparticles: The Influence of Size, Shape and Dielectric Environment" [45]. Therefore there is a strong requirement to develop non-invasive orientational imaging protocol.

3.2. Research Goals

In this experimental study, nanostructures were carefully chosen by analyzing them using transmission electron microscopy (TEM) and double beam spectrophotometer, localization techniques were employed in order to perform correlative microscopy, we have developed the correspondence between hyperspectral data and scanning electron microscopy using finely patterned substrate (via focused ion beam), and validation through finite-difference time-domain numerical simulation. Multiple points of interest can be mapped or characterized within the single image/sample.

3.3. Experiment

To investigate spectral shift in surface plasmon resonance of metallic nanostructures with respect to 2D orientation, polarized light is transmitted in Z-direction to excite Surface Plasmon Resonance.

Nanoparticles used in this research were manufactured by nanoComposix using large scale processing and concentration via filtering using cross-flow method. Polyvinylpyrrolidone (PVP) Silver Nanocubes were purchased from nanoComposix, Inc. UV-6300 Double Beam Spectrophotometer (line diagram in figure-8) is used to obtain the absorption spectrum of the nanocube sample. Extinction spectrum is negative log of intensity ratio of sample to reference.

$$S_{extinction} = -\log\left(\frac{I - I_{directcurrent}}{I_{reference} - I_{directcurrent}}\right)$$

Peaks obtained in the wavelength spectrum represent average line widths and resonance energy values as depicted in Figure-8. Several spectral features in the range 300-900 nm wavelengths are observed in the absorption spectra of the nanocube with the peak of the spectrum lying between 500-600 nm. Two prominent plasmon resonance peaks (468, 564 nm) are clearly visible (Figure 8). There are two resonance peaks with good features. Bigger peak depicts the strong resonance along long axis (lower energy) and smaller peak depicts the weak resonance along shorter axis

(higher in energy). This is because at longer axis, dipole moment is much stronger than the dipole moment at shorter axis.

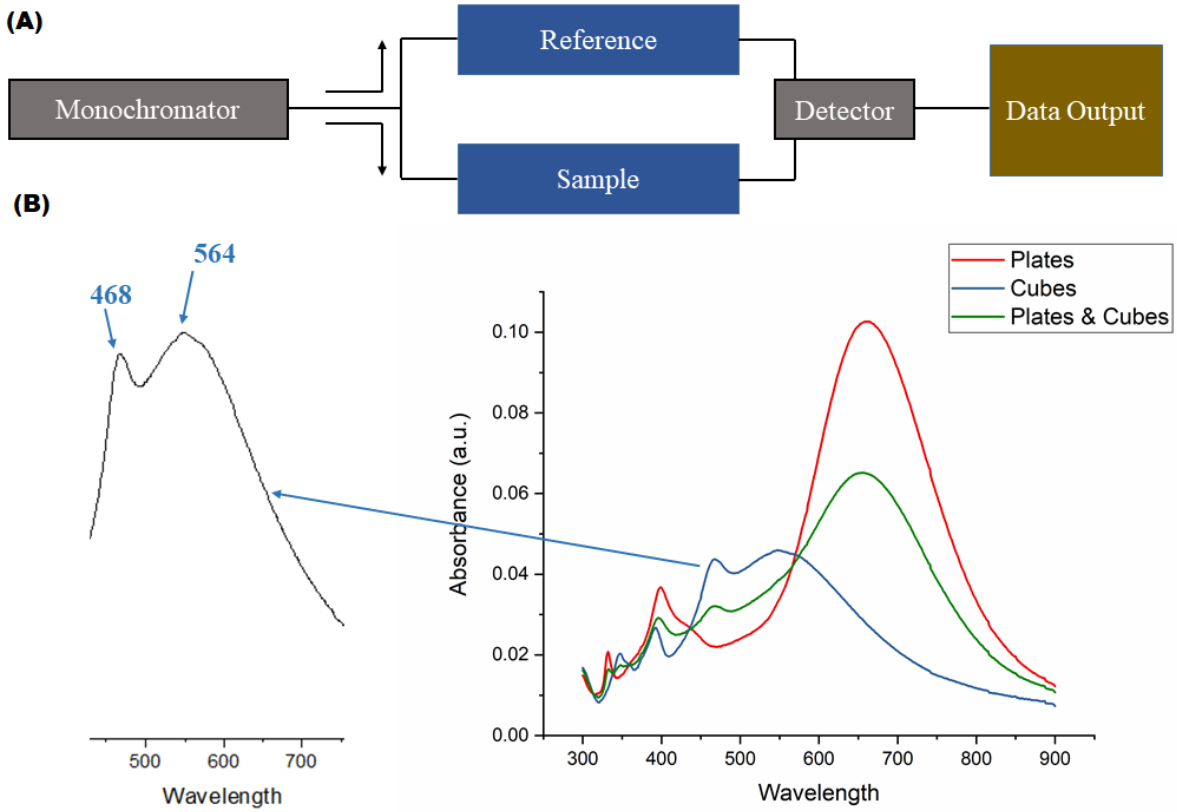

Figure 8: (A) Block diagram of absorbance double beam spectrophotometer (B) Ensemble spectra resonance distribution over the wavelength range 300-900nm

JEOL JEM-2011 high resolution Transmission Electron Microscopy (TEM) equipped with Gatan SC1000 CCD camera is used to conform shape and size distribution of the nano-particles. This procedure was performed to select nanoparticles with maximum symmetry for detecting orientation of a nano-structure via scattering spectroscopy as shown in Figure-9. Four different plasmonic structures were analyzed, namely gold micro-structures, silver nanocubes, gold nanorods, and silver nano-plates. It was observed that silver nanocubes were highly symmetric and consistent in shape and size. Transmission Electron Microscopy analysis of silver nanocubes was done in order to determine the average size distribution of the particles as shown in Figure-10.

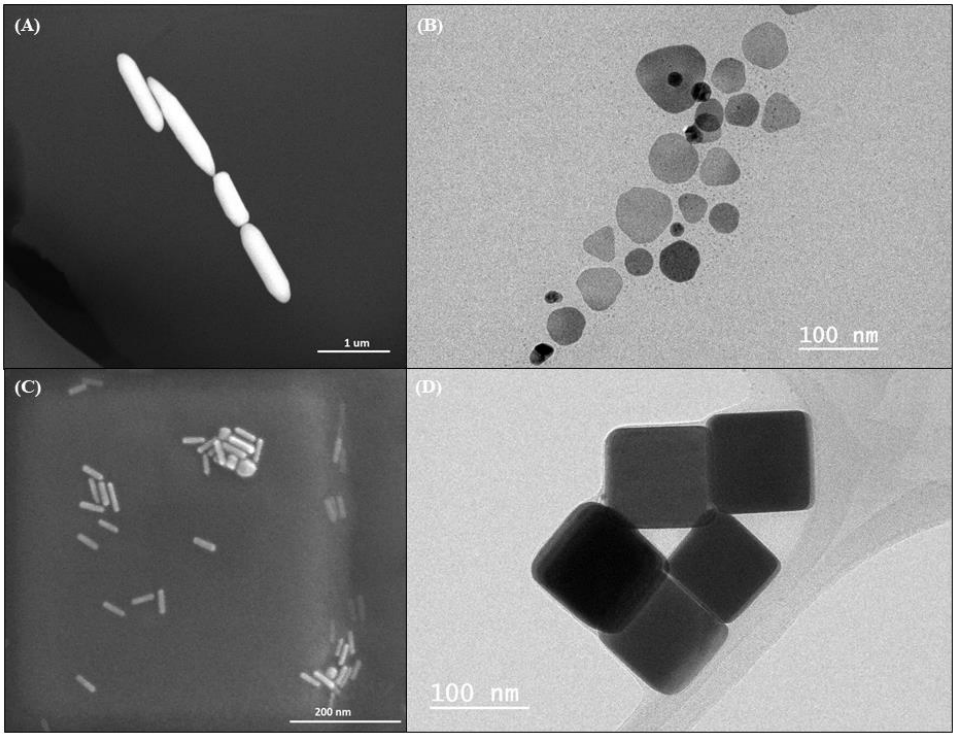

Figure 9: (A) Gold Micro rods (B) Silver Nanoplates (C) Gold Nanorods (D) Silver Nanocubes

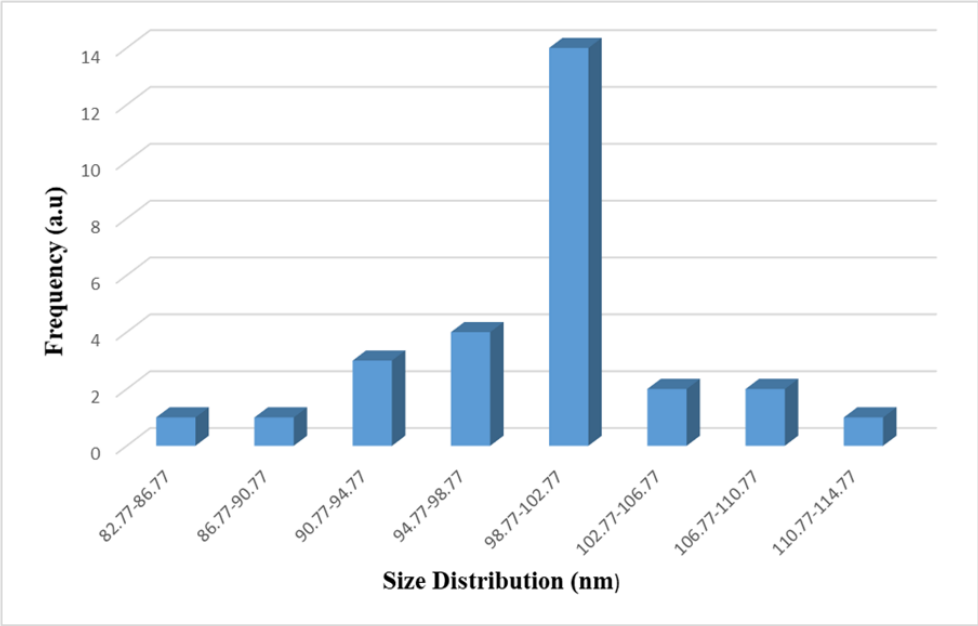

Figure 10: Size distribution of 30 silver nano-structures with frequency distributed over 8 bins

From the TEM image analysis of 30 silver nano-cube particles, the average diameter of the nanocubes with standard deviation was calculated to be 99.5±5 nm. Histogram depicts bell-curve.

Nano coupling effect in the plasmon resonance of the nano-structures is observed when distance is less than two or more plasmonic particles (edge-to-edge one particle diameter or less). Oscillating electrons on both the neighboring particles assume lowest energy state (similar to molecular orbital theory) and resonance red-shifts to longer wavelength (lower energy). Inter particle distance between nano-structures greatly influences the optical spectrum as shown in Figure 11. Blue or red shift is observed and becomes more prominent when it is compared with spectra from single nanostructure. Best concentration was designed at 0.01 mg/ml. Relationship is given by the following equation [46] where M=center-to-center distance and D=Diameter of the particle,

$$\in(\omega) = -\frac{8\left(\frac{M}{D}\right)^3 + 1}{4(\frac{M}{D})^3 - 1} \in_{media}$$

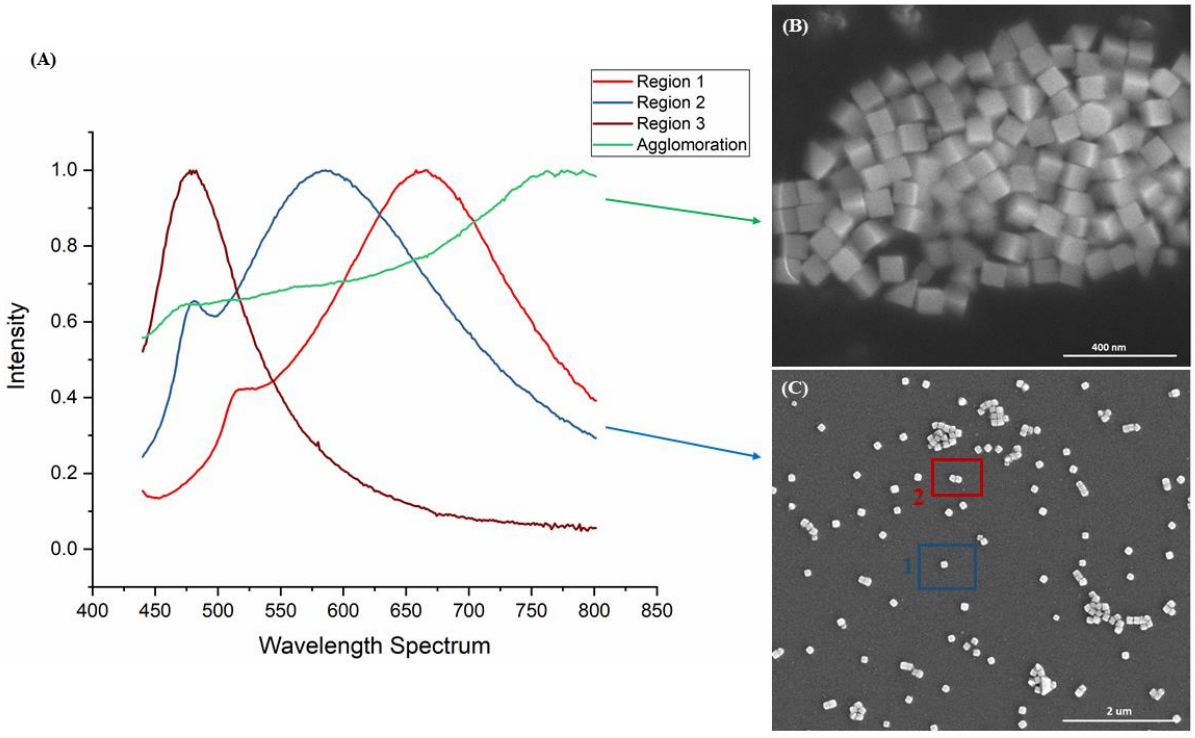

Figure 11: (A) Spectral response of single nano-particles, nano-coupled and agglomerated particles (B) 100 nm agglomerated silver nano-structures at 1mg/ml (B) Optimized concentration at 0.01 mg/ml

In the nano-particle localization, 2D Gaussian function is conveniently fitted to the intensity count at each wavelength of the Mie scattering from single nanocube vie equation [47]. Here I_0=intensity of background noise, A= amplitude of the Gaussian fitting function, x_0, y_0= central point of the pixel, and σ_x, σ_y= standard deviation of the intensity emitted.

$$I\left(x, y, A, I_0, x_0, y_0, \sigma_x, \sigma_y\right) = I_0 + A\exp[-\frac{1}{2}\left[\left(\frac{x - x_0}{\sigma_x}\right)^2 + \left(\frac{y - y_0}{\sigma_y}\right)^2\right]]$$

Particular attention was devoted to avoid particle agglomerations due to so called “coffee-ring” effect. Principle of “coffee ring effect” is the time-dependent contest between the particle mobility and vaporization of the liquid state of the solution [48, 49]. The coffee-ring effect can be avoided if during the drop-casting of the liquid nano-particle solution, the solution is vaporized well before reaching three-phase condition and capillary flow is prevented by constant stirring. Figure 12 shows the distribution of silver nanocubes (scattering images) on the unheated and on the heated substrate prior to drop casting nanoparticles solution. The environment is kept well below the oxidation potential for the metal nano-structures. Avoiding formation of coffee-ring structures greatly reduces the agglomeration of the nanoparticles, thereby preventing erroneous spectral data. Silver nanocubes were imaged again after 10 days of the initial experiment to confirm that the shape and size were unaffected due to environment and beam current before analyzing the same structures using hyperspectral imaging system.

In order to obtain precise information about intensity dots which can be seen in optical microscope as the light diffraction patterns of light scattered from the nano-structures, it is important to perform correlative microscopy as selecting the particles in optical microscope simply based on their intensity is not sufficient. Spectral libraries can be built to define characteristics based on physical features. Several methods can be employed in order to perform the correlative microscopy.

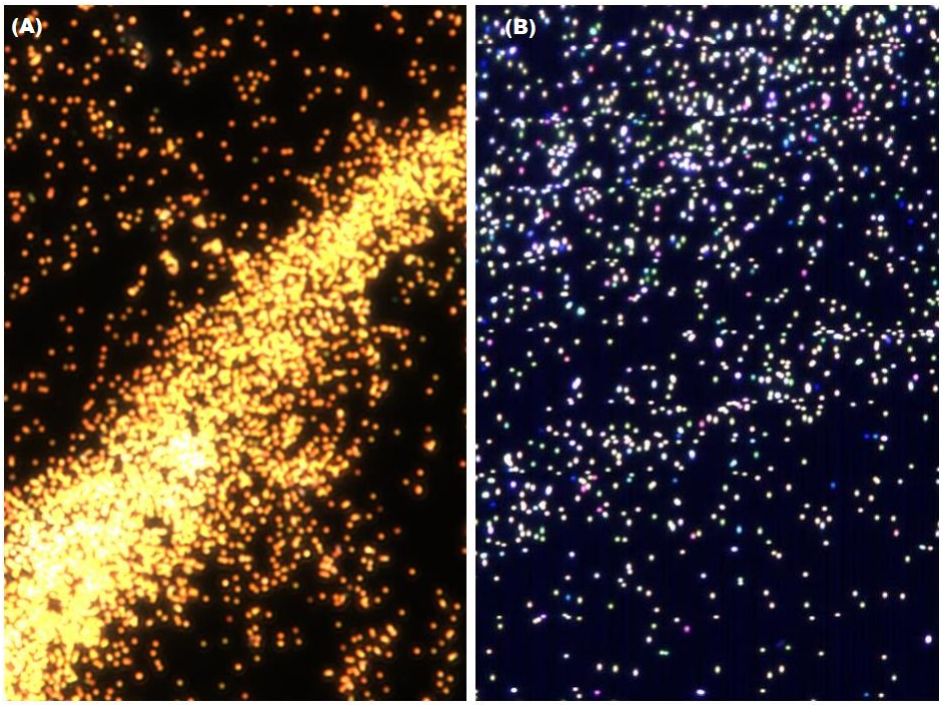

Figure 12: (A) Unheated substrate (B) Heated substrate at 50 degrees Celsius for 10 minutes and continuous stirring

Different techniques like nanosphere lithography, e-beam lithography, commercial patterned glass substrates, and focused ion beam milling were employed in order to determine and correlate location and orientation of a single nano-particle in SEM as well as in the hyperspectral optical setup.

Electron beam lithography is one of the popular methods where PMMA resist (950K) is spin coated at 3000 rpm for 45 seconds on the conductive film coated glass substrate. The protocol for e-beam lithography is depicted in Figure-13 A-D. Sample is then heated at 180 degrees for 45 seconds. Current value of 40 pA was utilized for writing user designed CAD patterns (5μm X 5 μm squares) on the substrate via NPGS (Nanometer Pattern Generation System) system. Substrate was developed in the solution to eliminate the exposed parts. During the experiment, while imaging the sample in SEM using electron beam, it was observed that the PMMA layer detached from the glass substrate and this is then washed away while drop-coating media containing nanostructures as shown in Figure 14.

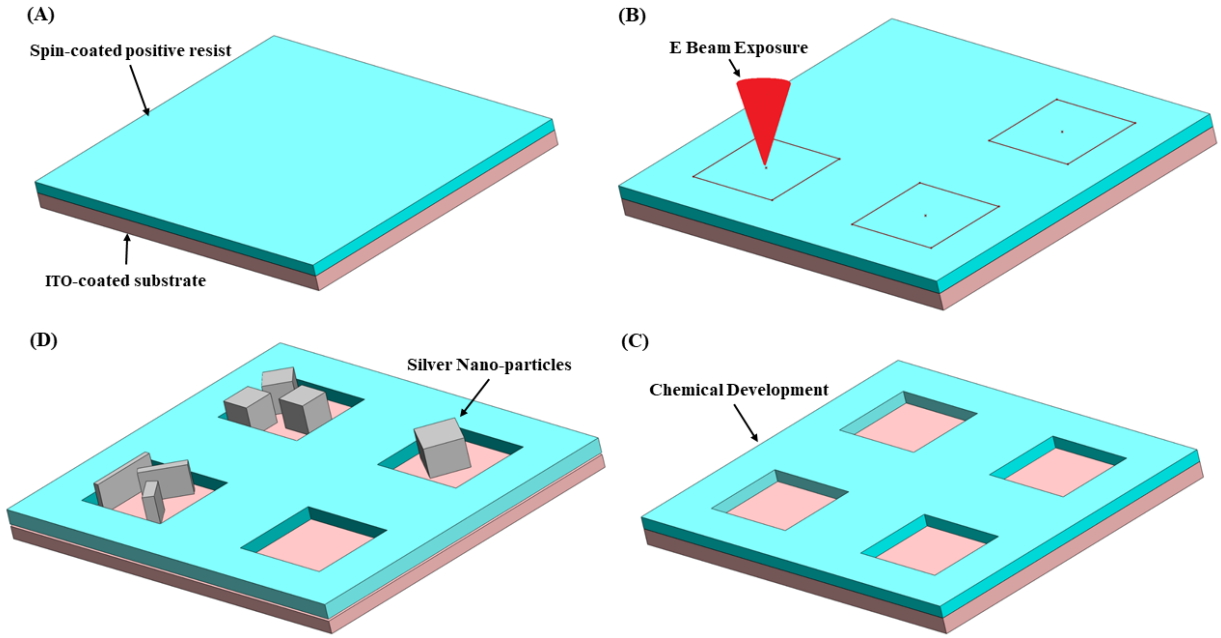

Figure 13: (A) PMMA resist spin-coated on ITO-coated substrate (B) E beam exposed on the resist for array of 5 μm X 5 μm area input by user defined CAD-file (C) Chemical development to detach and remove exposed areas (D) Drop-casting silver nano-structures to localize particles and determine their orientation

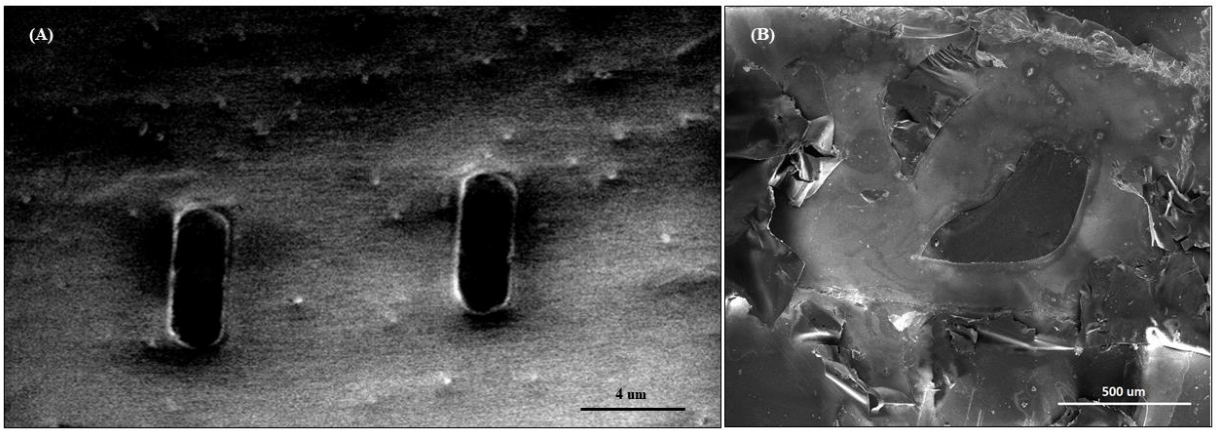

Figure 14: (A) 4 um X 4 um square structures generated using positive resist e-beam lithography (B) Peeling off of the resist due to fluid force and exposure to high intensity scanning electron beam

One of the effective and quick lithography techniques include nanosphere lithography in order to produce cost-effective and circular periodic arrays. Idea was to identify localized nano-structures and determine orientation via angles in a circle method by forming triangles and quadrants within the circular etched structures on the ITO-coated glass substrates. In nanosphere lithography,

polymer nanosphere of polystyrene material are drop-coated on the substrate via self-assembling technique. Using reactive-ion etching technique, markings in the glass substrate are carried out as shown in Figure 15.

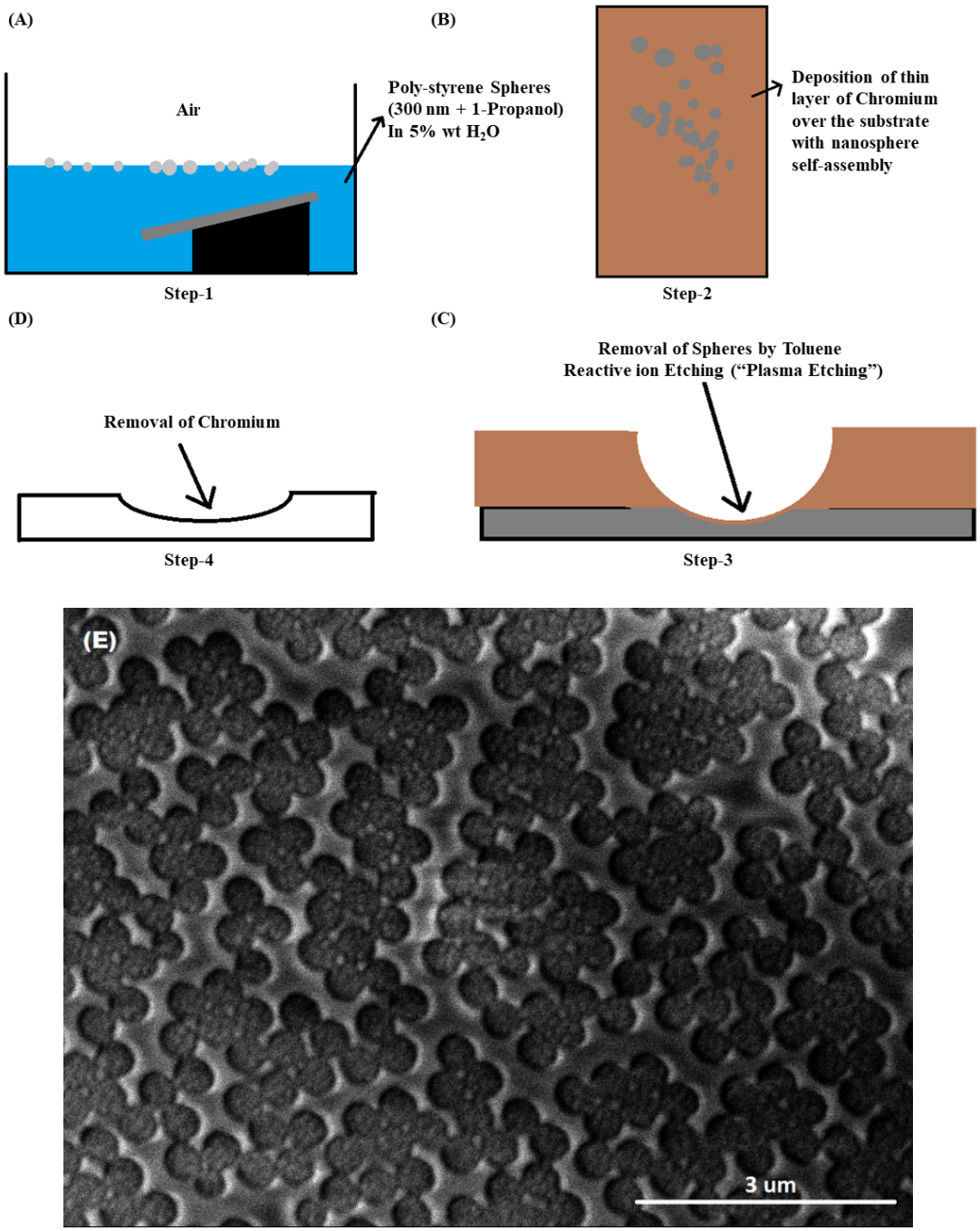

Figure 15: (A) 300 nm polystyrene nanosphere are carefully self-assembled on a substrate (B) Chromium is electro-deposited on the assembly (C) Nanosphere are removed via toluene and glass reactive ion etching is performed (D) Chromium removal (E) SEM image

In nanosphere lithography, etching of the glass substrate was obtained in a merged fashion and hence the localization of the single nano-structures was not efficient with this method.

In order to locate and study the same nanoparticle in the hyperspectral microscope and SEM successfully, Focused Gallium Ion Beam was used to make square arrays of X-Y dimensions 1-1.5 μm [50]. Focused Ion Beam (FIB) milling was used to generate sharp 90 degrees angled grooves of about 0.5 μm depth (using a high ion beam energy of 20 keV) as shown in Figure 16. Markings/Pattern were created using highly accurate processing step on glass substrate with Indium Tin Oxide (ITO) coating of 30 nm thickness which is finely deposited over the whole glass surface. ITO coating provides good conductivity for bombarded ions and thereby generating fine resolution milled nano-patterns avoiding filleted edges due to charge localization inside vacuum chamber. Substrate is placed on the 5 directional motor controlled stage and milled by orienting the sample at 51 degrees. FIB is similar to electron beam except that beam is gallium beam. When the Ga ions hit the substrate, energy transfer takes place. Breaking of bonds for substrate occurs due to intense energy and high atomic momentum due to extraction voltage at 7000 V. Milling is carried out in the vacuum chamber. Benefit of patterning using FIB micromachining includes super-resolution achieved <100 nm.

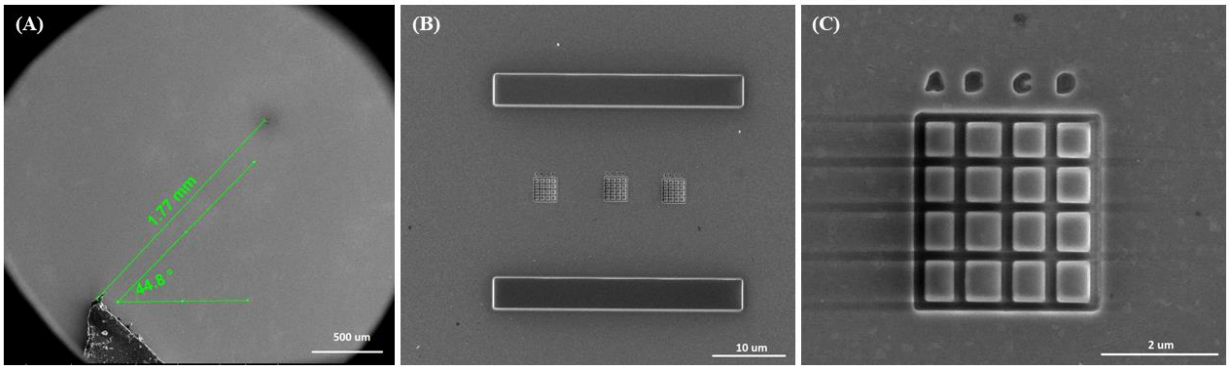

Figure 16: (A) Carbon tape marking to identify field of view at 50x magnification (B) Thick grooves of 2 um depth and thickness viewed at 2500x magnification. Milled to locate arrays during optical microscopy and SEM imaging (C) At 20,000x magnification, Sharp 90 degrees angled grooves of about 0.5 μm depth

Micro-milled glass substrate is preheated in oven to 50 degrees for 10 minutes before drop-casting particles in order to prevent coffee-ring phenomena in nanostructure distribution by quick elimination of solution water. 5 µL solution containing silver nanoparticles was drop-coated on indexed glass slide and water was allowed to vaporize. Electron Beam analytical tool such as Scanning Electron Microscopy (SEM) was used to determine angular orientation of nanostructure with respect to indexed grid substrate. Two dimensional angular orientation of particles was then analyzed with respect to parallel features in Image J software. Optical microscopes are diffraction limited (250 nm) and therefore image viewed in hyperspectral dark field imaging system appears 10x more magnified than SEM image as shown in Figure-17.

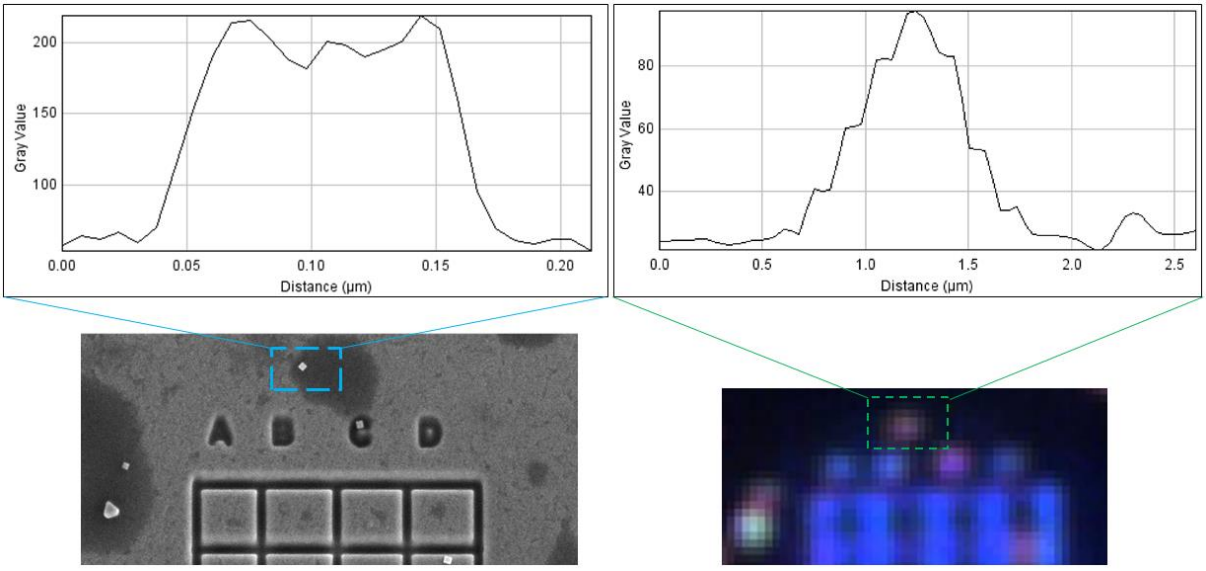

Figure 17: Pixel to distance comparison between SEM image and the hyperspectral image. Hyperspectral image is 10x the SEM image.

Color of concentrated gold nanostructures appears red in color as it has strong absorbance and scattering value in green region of spectrum. Whereas solution of silver appears yellow in color due to strong scattering and absorbance properties in blue region of the spectrum. Only particular wavelengths of light can drive the phenomena known as surface plasmon resonance (SPR).

Wavelength at which incoming photons are absorbed are not emitted in the scattering spectrum. Dipole oscillation of electrons is induced at specific wavelengths.

CytoViva Hyperspectral Microscope with hyperspectral imaging modality in the visible near-infrared range (400-1000 nm) was used. High intensity halogen light source is focused at oblique angles through the liquid light guide and illumination condenser. Spectral resolution of 2 nm and spatial pixel width of 25 nm was achieved using the system. Oil objectives with 100x magnification were used in our experiment in order to obtain high resolution images as shown in Figure-18. Immersion oil contributes in reducing the speed of light thereby shortening the wavelength while at the same time keeping frequency constant. According to relation $\lambda = 2\pi c/\omega$, where c is speed of light and ω angular frequency [33]. Polarizing filter was placed between condenser and glass substrate in order to minimize random glare. Particles were sandwiched by gently placing coverslip over the substrate and fixing the same by using colorless nail-polish to avoid oil-interaction. Care is taken to not allow air-bubbles between cover-slip and glass substrate. Exposure for each pixel is set constant at 0.25 sec.

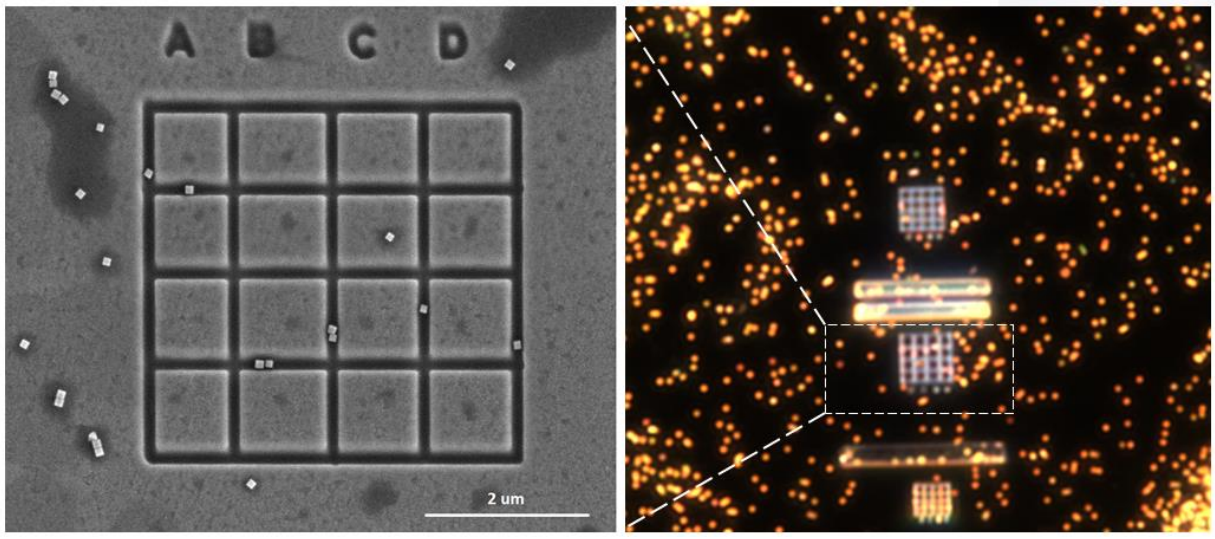

Figure 18: Dark-field optical image at 100x correlated with SEM image of the same array (drop-coated with silver nanocubes)

Hyperspectral spectrograph was used to collect spectral data at room temperature and intensity count adjusted between 1000 and 10000 in order to minimize noise. Images were processed using ENVI 4.8 software (CytoViva®, Inc.) in dark-field mode. Spectral information of nanoparticles obtained from experiments and simulation are normalized to maximum intensity value of 1 as shown in Figure-19.

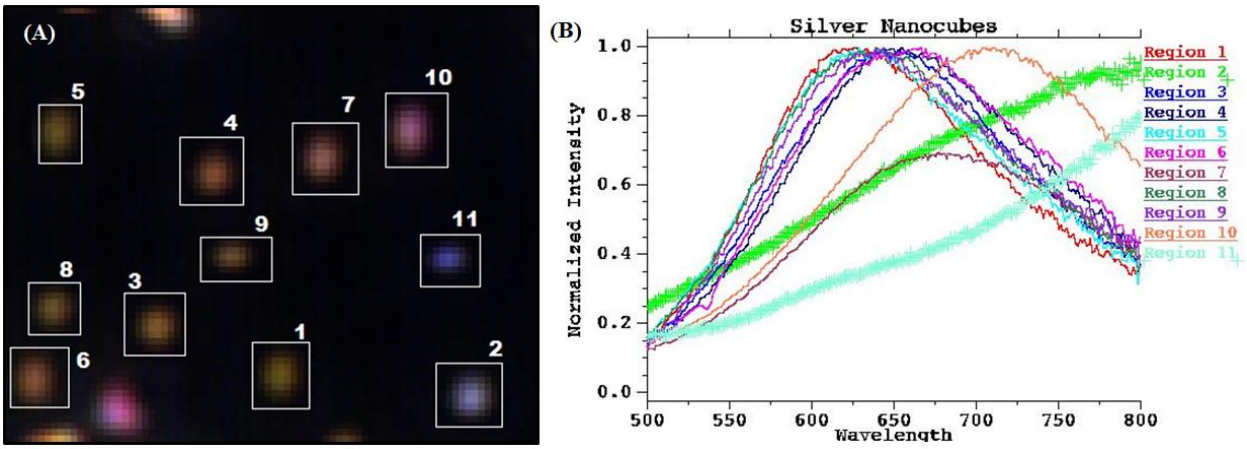

Figure 19: (A) Nanostructures as seen in dark-field hyperspectral image (B) Spectral distribution over the wavelength an3d intensity normalized to 1

Regions of Interest are carefully selected from the particles which can be correlated within SEM image and hyperspectral image to collect spectra from pixels that contain information from individual nanostructures after carefully subtracting background irregularities. In this hyperspectral modality, information is collected one row of pixel at a time by raster scanning over the whole field of view. This method is identified as a pushbroom method. The grids patterned using FIB are marked with letters A, B, C, D in order to correlate exact position of nano-particles as shown in Figure-20. Geometrical axes X and Y of the dark-field image matches with the patterned grid structures horizontal and vertical axes. No special tagging or staining was done for 100 nm silver nanoparticles. Hyperspectral Images are corrected for normalized incident lamp spectrum. Lamp correction, $I = \frac{I_{sample} - I_{background}}{I_{light} - I_{background}}$

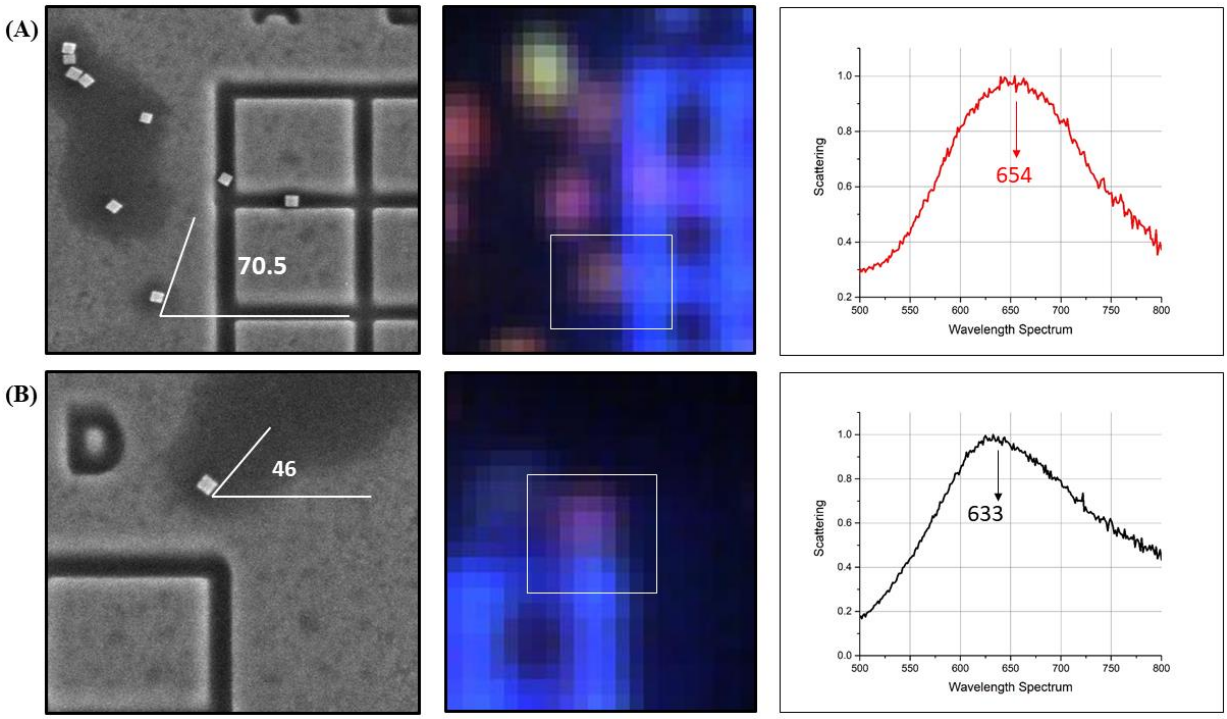

Figure 20: Correlative analysis between SEM image and hyperspectral image along with corresponding spectral signature of the single nano-particle (A) oriented at 70.5 degrees (B) oriented at 46 degrees

Additional methods to numerically discretize the electromagnetic interaction with the object in study have been developed by the researchers. Two major theories to numerically calculate electromagnetic spectrum are discrete dipole approximation and the finite-difference time-domain methods. We have used time domain discretization for the calculation of spectral data of N-number of polarizable small elements. These elements interact with incoming incident light. For elements with arbitrary shape and size, solving Maxwell's equation [51] in time domain gives good results for the particles of interest.

$$\text{Time varying electric field,} \quad \frac{\partial \mathrm{E}}{\partial \mathrm{t}} = \frac{1}{\epsilon_o} \nabla \mathrm{X\ H}$$

$$\text{Time varying magnetic field,} \quad \frac{\partial \mathrm{H}}{\partial \mathrm{t}} = -\frac{1}{\mu_o} \nabla \mathrm{X\ E}$$

Figure 21 shows the Finite difference time domain simulation results. Finite-difference time-domain (FDTD) simulations were performed by utilizing Lumerical FDTD Solutions. The

refractive index of silver was obtained from CRC data [52], and the refractive index of glass was chosen 1.51. The mesh size was chosen 2 nm throughout the simulation domain which was terminated to perfectly matched layers (PML) in all directions. A plane wave (Total-Field Scattered-Field) was used to excite the nanostructure as the pump signal (normally incident from top) in the wavelength range of 400 nm to 900 nm. The local electric field distribution in the surface of nano-cube at the resonance frequency was obtained using a plane frequency-domain field monitors on all sides.

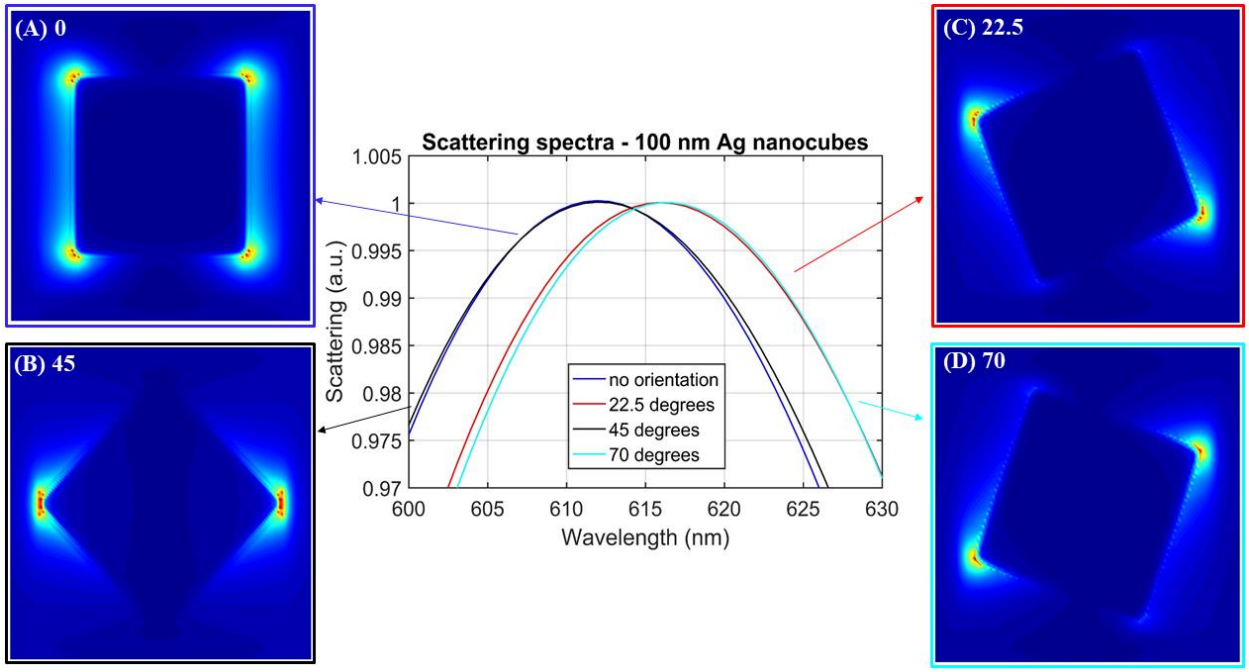

Figure 21: Finite-difference-time-domain simulation results depicting electro-magnetic distribution (due to dipole moment) and resonance for the light incident on the silver nanocube oriented at (A) 0 degrees (B) 45 degrees (C) 22.5 degrees (D) 70 degrees

3.4. Results and Discussion

Single particle spectral analysis in hyperspectral microscope is possible due to conversion of electromagnetic energy in electrical signals using Fourier transform spectrometer situated at focal point in the optical setup. Imaging conditions were kept same for all the hyperspectral images. Figure-22 shows spectral distribution of the scattering wavelengths emitted by the surface plasmon

of a single particle by defining precise region of interest for single nano-structures oriented at different angles. We observe that the spectral peak lie between 652-657 nm when the orientation of nanocubes is around 70 and 22.5 degrees with respect to the horizontal polarization direction; whereas the spectral peaks blue-shifted to 630-635 nm when orientation of the cube is approximately about 0 or 45 degrees.

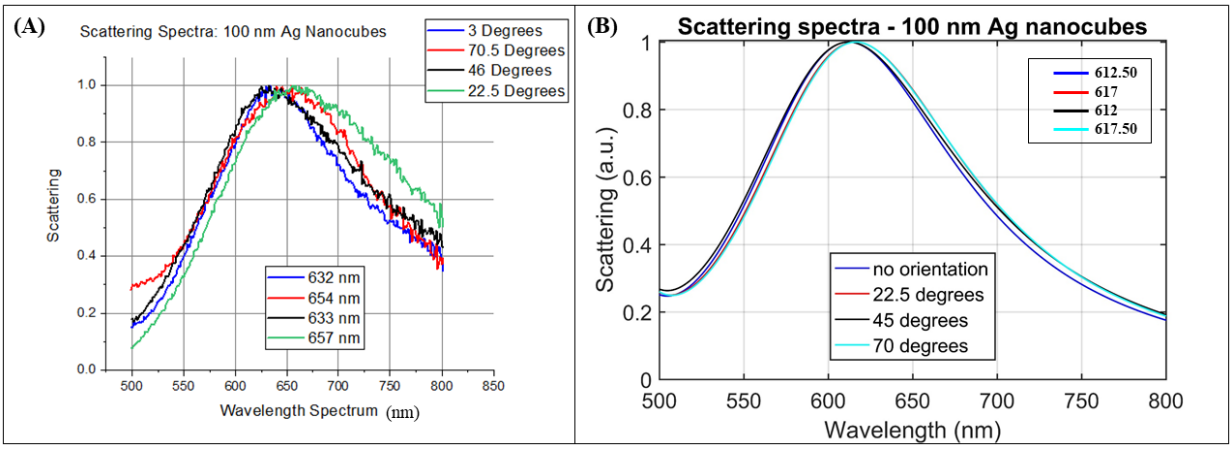

Figure 22: (A) Plasmon resonance experimental spectra from the cubes oriented at 3 degrees, 70.5, 46, and 22.5 degrees is compared against (B) Simulation spectral results at 0, 22.5, 45, and 70 degrees

We observe red-shift in spectrum by 12-15 nm when particles are oriented between $15<\theta<35$ and $60<\theta<80$. When the orientation of the particles changed from 70 to 45 degree, the FDTD results showed a spectral blue-shift (Figure 22) confirming our experimental observation. Redshift of about 5 nm is observed for angles closer to 22.5 ($0<\theta<45$) and 70 ($45<\theta<90$) in both experiments and simulations due to inhomogeneous polarization. Wider spectral shift could be expected for less symmetric objects compared to nanocubes (for example, gold nanorods). This close correspondence between FDTD simulation and experimental results allows us to expand the scope of developing precise libraries in hyperspectral system for quick, label-free and cost efficient analysis of nanostructures. Differences in the value of spectral-shift in the experimental data and simulation results may be due to the surface roughness of the particles that are not captured in the FDTD simulation set up. There is no noticeable broadening of plasmon linewidth because particle

size remains constant and same. While there is red-shifting of the wavelength observed which implies there are retardation effects and incident light cannot be polarized homogenously.

CHAPTER 4: NONINVASIVE SINGLE STEM-CELL DIFFERENTIATION ANALYSIS

4.1. Literature Review

In this research, we have developed cost-effective and non-invasive imaging methodology to study the single-cell differentiation process of human adult stem cells (ASCs) into osteocytes and adipocytes. Adipose derived mesenchymal stem cells (ASCs) can be used for multiple regenerative medicinal purposes as shown in Figure 23.

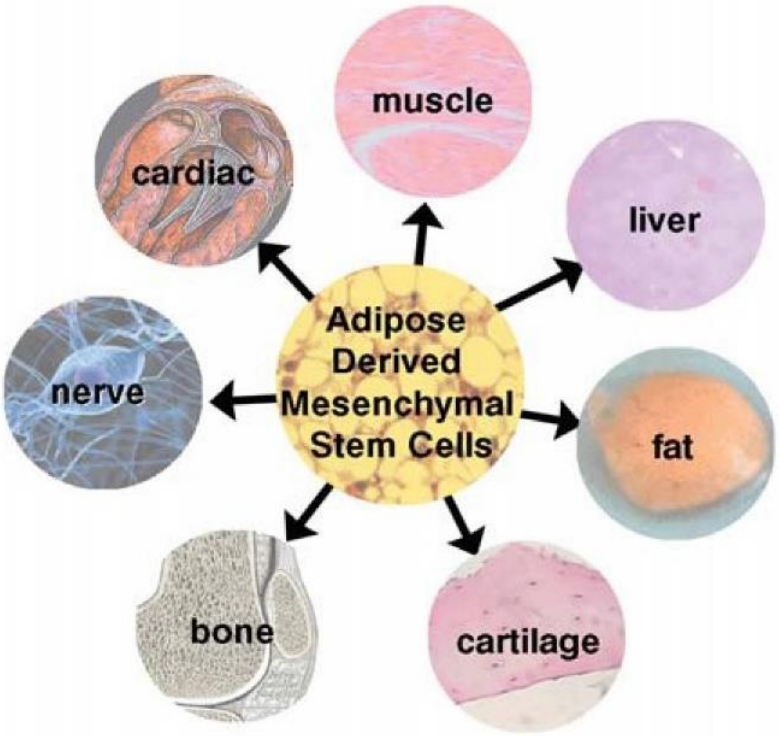

Figure 23: Application of Adipose Derived Stem-cells (ASCs) in regenerative therapies [53]

Although individual cells in a particular organ, tissue or cell culture may be morphologically and genetically identical, they are heterogeneous in nature. Some of the most commonly used single-cell imaging techniques include differential interference contrast (DIC), SEM, AFM, laser scanning confocal fluorescence microscopy, fluorescence cross-correlation spectroscopy and matrix-assisted laser desorption/ionization-mass spectrometry [54]. The primary advantage of HSI

over these techniques is an ability to allow for a more accurate segmentation and classification of the acquired image. For example, in cellular imaging, taking into account only mono-chromatic color change to detect abnormalities is always not enough as certain bio-phenomena might not produce significant optical contrast. HSI offers a significant advantage by storing the value of an entire spectrum within one single pixel in the image along with the precise spatial (location) information. As is well known, biological cells are composed of different subcellular level organelles varying in size that ranges from a couple of nanometers to a few tens of microns. Scattering and absorption of light from each of these minor components are mainly dependent on their molecular composition. Refractive index of the components such as fatty acids which find a match with index of HSI microscope objective lubricant show extremely redundant high-noise spectra whereas organelles such as mitochondria are the dominant scatters. Scattering spectra variation from the cellular walls in mainly due to structural formation against molecular composition [26]. Hence the absorbed, scattered, and transmitted light from the biological sample captured by HSI at a resolution less than 50 nm can capture spectral data from minute components of a single cell. This facility till date cannot be efficiently achieved in spectroscopy, RGB or monochrome.

As noted earlier in chapter-2, a primary requirement for the use of HSI is a reference library (or prior knowledge of the optical-radiative properties of the control samples). Fortuitously, an extensive body of supporting literature exists to describe the optical properties of biological samples (such as absorption and scattering in tissues, fluorescence anisotropy, diffused scattering, and refractive index modulation within cells) and their properties/values have been extensively studied and tabulated [55-57]. An excellent review by Jacques [58] calculates the anisotropy, g, to characterizes the effective scattering in tissues in terms of optical absorption coefficient (μa),

average hemoglobin concentration in the tissue, scattering coefficient (μs), and angle of scattering ($p(\theta)$). Jacques [58] argues that "generic tissue" properties may be adequate, but not sufficient to address subject specific, temporal and variations between patients. Thus, accurate prediction(s) will necessitate real-time optical property quantification when working on individual patients as well as in analyzing the *in vitro* response of cell populations, a task which HSI is uniquely qualified to accomplish.

Extensive literature exists for single cell analysis of cancer cells and tissues. Here we will focus on the monitoring and quantification of stem cell functionality, viability and/or differentiation. Controlled differentiation and maintaining the purity of differentiated cells are two of the most important challenges today in stem cell research. For example, it is important to monitor stem cell differentiation carefully for clinical application as undifferentiated implanted cells may lead to teratomas. Routinely used methods include cell staining and flow sorting techniques; cell staining can be tedious, laborious and error-prone if improperly handled or assessed, while cell sorting techniques are quite fast and quantitative but are population/average based and are unable to capture cell to cell variations and spatial variations within the cell sample. Additionally, due to photo-bleaching and photo-stability issues, the cell-sorting technique cannot readily be translated for use with long-term cell differentiation studies. Both these techniques, cell staining and flow methods are also damaging and rate-limiting processes, i.e., cells utilized for these assays are treated as waste materials and unable to be processed further. Thus, additional matching and duplicate/representative samples need to be prepared for parallel biological assays (e.g. RNA, cDNA analysis) studies. For example, to monitor the progression of osteogenesis in stem cells, at different time points requires, multiple cell cultures with a concomitant reduction in efficiency and an increased use of costly operational resources [59].

In general, spectroscopy based techniques are also ideally suited to address the challenge of stem cell sorting and to ensure their purity. Currently available and magnetic bead-based cell sorting assays are limited and cell specific, and sub-optimal for therapy. Hence there is a need to develop techniques that are non-invasive, sensitive, easy to use and rapid, to analyze single cells as well as to monitor or sort through a population of cells. Specifically, a HSI based spectroscopic mapping method has the potential to rapidly and non-invasively monitor cell differentiation. The usage of spectroscopy-based techniques will also allow for a direct correlation between the osteogenic (mineralization) data and RNA/cDNA analysis. This capability has the potential to significantly improve the robustness and sensitivity of cell differentiation studies. In addition, by combining microfluidic devices and technologies to the spectroscopy based techniques, the HSI system can achieve high-throughput screening as well as sorting-based assays [60].

Vermaas et al. [61] combined fluorescence and a label-free Raman spectroscopy technique (resonance Raman scattering) to visualize carotenoid within the cell wall and the membranes of live photosynthetic (*Synechocystis)* cells. Vermaas et al. [61] utilized the hyperspectral confocal fluorescence imaging system along with multivariate curve resolution (MCR) algorithms to achieve a spatial resolution that is diffraction-limited (~ 250 × 250 × 600 nm). Vermaas et al. [61] were then able to distinguish and analyze the maximum intensity of the fluorescence spectrum that was only 10–15 nm apart and also illustrated the confidence level of multivariate data by analyzing the signal-to-noise ratio of the experimental data as well as the level of the agreement between the experimentally collected and the simulated spectra. Thus, this MCR based approach by Vermaas et al [61] allowed for a thorough analysis of each fluorescent component and their intensities compared to each other within a single cell in three dimensions. Interestingly, Haaland and Thomas [62] suggest an improvement over the MCR algorithm by using partially constrained models

instead of the fully constrained MCR models. Haaland and Thomas [62] applied the new partially constrained algorithm to fixed lung epithelial cells as well as to images of mercurochrome-stained endosperm portions of a wild-type corn seed and showed improved interpretability of the results. Thus, careful attention to the modalities of the MCR algorithms is required when analyzing the hyperspectral imaging data [63].

It is worth mentioning that, besides HSI, other spectroscopy techniques are also capable of doing single stem cell analysis with high spatial (x, y) resolution. Here, we will mention two of those techniques such as non-linear Raman spectroscopy imaging and surface plasmon resonance imaging. Those two techniques are chosen here as they are capable of performing video-rate acquisition similar to HSI. Wang et al. [64] presented a new label-free technique called electrochemical impedance (EIM) based on Surface Plasmon Resonance (SPR). SPR are surface waves at a metal/dielectric interface due to the collective oscillation of free electrons, reported first by Wood in 1902 [65]. Subsequently, in 1968 both Otto [66] and Kretschmann & Raether [67] showed that SPR can be generated on a glass-metal interface using two different configurations. In the Otto's configuration the thin metal film is separated from the glass block (prism) through which light with a precise wavelength and incident angle can undergo total internal reflection to generate SPR. In the Kretschmann and Raether's set up the thin metal film is evaporated on to the glass block (prism) through which light with a precise wavelength and incident angle generate SPR. SPR is highly sensitive to refractive index changes and hence, can be utilized as a sensor. However, the effectiveness of SPR lies within the penetration depth of the evanescent wave (typically ~ 200 nm). The EIM method developed by Wang et al. [64] is based on the inter-dependence between SPR and the surface charge density as opposed to changes in refractive index resulting from the molecular binding process [68]. By simultaneously recording the optical, SPR,

and EIM images Wang et al. [64] studied the induction and progression of cellular apoptotic events in the human papilloma virus 16 infected cervical Si-Ha cell line as well as electroporation in individual adherent cultured mammalian cells. Wang et al. [69] then imaged the cell-substrate interaction on a single cell with a resolution that is finer than the dimension of a cell. By varying the osmotic pressure from 300mOsm to 350mOsm (achieved by varying the concentration of mannitol in solution) they measured the associated SPR intensity changes. By postulating that the larger displacement obtained from the SPR intensity changes signifies smaller adhesion strength they mapped the local adhesion strength of the cell to the substrate. Thus, the EIM method allowed Wang et al. [64] to monitor with sub-micron spatial resolution the dynamics of apoptosis and electroporation of individual cells with millisecond time resolution.

Current SPR imaging (SPRi) is typically achieved by scanning the laser and collecting the surface plasmon wave light using a microscope objective. SPRi can be generated through evanescent wave coupling of prism excitation or free wave coupling with metallic nanostructures. Being a label-free imaging modality, SPRi preserves the integrity of the cells and allow observation of external and internal cellular processes (within a penetration depth). So far, SPRi has been used for cell adhesion and basic cell biology studies [70] and for rapid and accurate detection of bacteria at low concentrations in health and food industries [71]. More importantly, these studies provided statistically significant data through the analysis of individual cells [72]. Thus demonstrating that SPRi is capable of providing high spatial resolution required to perform single-cell level analysis as well as providing a wide field-of-view to observe a statistically significant number of cells concurrently within the analysis zone [73].

Building upon these early studies, recent advances in dark field-based HSI techniques represent an encouraging analytical tool for investigating objects that scatter efficiently (e.g. nanoparticles)

in bio-systems. As stated earlier, HSI is capable of combining imaging with spectroscopy, thus allowing for the positive identification of the location and distribution of unknown nanoparticles in vivo or ex vivo [21]. Other advantages of using HSI systems over conventional imaging techniques include minimal and non-destructive sample preparation, rapid image acquisition and analysis, a relatively cheap and cost-effective system, and the ability to determine the spatial distribution and identification of materials in complex matrices (with known or custom-built reference libraries) [21]. HSI has also been successfully applied to provide real-time images of biomarker information and to analyze cell pathophysiology based on the spectral resonance characteristics of relevant tissues. Therefore, the use of HSI for medical diagnostics and image guided surgeries is on an upward slope. HSI has been reportedly used for the diagnosis of peripheral artery disease, the assessment of hemorrhagic shock, early recognition of dental decay/cavities, faster classification of kidney stones, and in detecting laryngeal disorders as briefly described below.

As it stands, HSI spectral imaging is sufficiently validated as a modality for *ex vivo* Aβ aggregate detection in mouse brain and retina, *in vitro* screening of chemical entities for amyloid genesis modulatory activity [25]. These findings have served as the basis for an extensive ongoing program on *in vivo* HSI imaging of live mouse/human retina [25, 74]. Taking advantage of the plasmonic nano-probes with characteristic localized SPR, Wang et al. [23] have demonstrated the capability of a dark field HSI method for quantification and mapping of multiple epigenetic marks at a resolution which allows this analysis in single cells. The dark field HSI was used for breaking the spatial diffraction limit and improved the low signal-to-noise ratio associated with quantification of cytosine modifications using fluorescence microscopy. Fluorescence microscopy is one of the most widely used optical methods for *in situ* visualization of biological molecules at the cellular

and molecular levels. Compared with fluorescence microscopy, the dark field HSI approach suffers minimally from errors associated with auto-fluorescence, photo-bleaching, and photo-toxicity [23].

HSI has also been utilized to study the dynamics inside a single cell. Chaudhari and Pradeep [75] demonstrated the use of polarized HSI to track rotational dynamics of gold nanorods inside live HEK293 cells. This study [75] provided a method to assess and for improved understanding of the state of an anisotropic nanostructure in complex environments. These observations in three-dimensions of intracellular rotational dynamics of gold nanorods represented a new landmark in single particle scattering spectroscopy [75]. Subsequently, Oh et al. [28] visualized and quantified the distribution of cellular iron using an intrinsic hyperspectral fluorescence signal to analyze the physiological role of iron in substantia nigra and its relationship to the progression of Parkinson's disease. The availability of commercial software for analyzing hyperspectral images has significantly enhanced the ease and access of HSI systems and exponentially increased the number and variety of biological problems that can be addressed. For example, Verebes et al. [76] obtained unique spectral signatures of red blood cells (RBCs); while Mortimer et al. [77] examined the uptake of different metal-based nanoparticles/quantum dots at concentrations in the ciliated protozoan Tetrahymena thermophile.

In addition to the fast cellular dynamics study mentioned above, HSI was also utilized to investigate drug delivery over a longer time scale. Misra et al. [78] performed HSI imaging to quantify and detect sub 30 nm phospholipid stabilized nanoparticles without the use of a fluorophore. The spatial and temporal resolution permitted by HSI allowed Misra et al [78] to detect and quantify the delivery of drugs from these nanoparticle carriers inside a 3-dimensional MCF-7 breast cancer cells. Conti et al. [24] developed a protocol for imaging of healthy RBCs

using a dark field HSI technique and developed a specific spectral library to analyze the composition of RBCs. As described by Conti et al. [24] the spectra correctly characterized the erythrocyte components such as the membrane and sub-membrane regions. Such precision in mapping cellular components is promising for the future use of HSI for the analysis of single molecules, small or large proteins, and the membrane phospholipid assembly [24]. HSI has also been reported for the identification of stem cell subpopulations [79], diabetic tissue diagnostics [80], and evaluating the condition of preimplantation embryo [81]. Briefly, Gosnell et al. [79] detected genetic mutations in cancer (or CD90 expression) using novel image processing techniques along with a multispectral wide-field fluorescence microscope while Khoadiar et al. [80] demonstrated that HSI has the capability to identify microvascular abnormalities and oxygenation patterns in diabetic foot.

4.2. Research Goal

To develop and refine non-invasive and cost-effective dark-field imaging protocol coupled with hyperspectral spectroscopy in order to study the differentiation of adult human stem cells (ASCs) into osteoblasts and adipocytes. ASCs undergoing adipogenesis (at days 3, 6 and 9 of the cell-culture) and osteogenesis (at days 7, 14 and 21 of the culture process) are monitored. Unique biochemical signals within control and differentiated cells are identified via matrix assisted laser desorption/ionization spectroscopy. Spectra collected from the pure chemicals are then mapped on hyperspectral images via spectral angle mapping algorithm and map density is obtained for the control and differentiated cells. Additional image analysis technique like template match algorithm is explored in order to complement spectra based sorting protocol. In future, techniques like confocal fluorescence imaging and Raman spectroscopy, gene expression experiments can supplement the quest of developing full-proof stem cell differentiation analysis protocol.

4.3. Materials and Methods

Cell culture - Frozen-thawed ASCs plated on 12 well-plate at a density of 3 X 10^4 cells/cm^2. Sample was delivered in salt-media to let the cells remain alive. Sample was analyzed within 2 hours of ejecting out of stromal media in order to obtain good results. Stromal media for control consist of DMEM, FBS, and FB. In order to induce growth characteristics for differentiation, more chemicals are added over the sample containing stromal media which can been inferred in detail from Table-1 and Table-2.

Table 1 - Constituents of the adipogenic differentiation cell-culture

Adipogenic Differentiation		
Stromal Media for Control	DMEM, FBS, AB	
Stromal Media + Chemicals for Differentiation	DMEM, FBS, AB+ (changed concentration)	Up to Day-3: Biotin, Pantothenate, Bovine, Insulin, Dexamethasone, IBMX, Penicillin, Rosiglitazone After Day-3: Omission of IBMX and Rosiglitazone
Differentiation Secreted Molecules	RUNX2 and PPAR-c proteins, Tissue proteins like inter-Leukins and TNF-a (inflammatory cytokines)	Adiponectin, Adipsin, Apelin, apolipoprotein E, leptin, glycerol 3—phosphate dehydrogenase

No bio-markers were infused into the sample in order to probe non-invasively.

Table 2 - Constituents of the osteogenic differentiation cell-culture

Osteogenic Differentiation		
Stromal Media for Control	DMEM, FBS, AB	
Stromal Media + Chemicals for Differentiation	DMEM, FBS, AB+ (changed concentration)	10 mM β-glycerophosphate, 50 μg/mL L-ascorbic acid 2-phosphate sesquimagnesium salt hydrate, and 10 mM dexamethasone
Differentiation Secreted Molecules	Aggrecan, Alkaline Phosphate/ALPL, Biglycan, Collagen I, Decorin, DMP-1	Fibronectin, Fibronectin/ Anastellin, IBSP/Sialoprotein II, Hydroxyapatite, IGFBP-3, IGFBP-RP10, MEPE/OF45

Sample preparation - Parallel sample preparation with 4% paraformaldehyde + oil o red (adipocytes) and 70% ice cold ethanol + 2% alizarin red solution (osteocytes) is carried out in order to perform inverted optical microscopy and check bulk sample growth characteristics as shown in Figure-24. This step in the sample preparation provides qualitative information regarding health of the differentiating donor cells.

3 μL solution was drop-casted on the glass substrate and sandwich structure was generated by placing the cover-slip over it. Sealing was done using colorless nail-polish in order to prevent oil interaction. Here we use label-free sample. Traditional invasive method includes staining the cells with oil-o red in order to differentiate them from control sample.

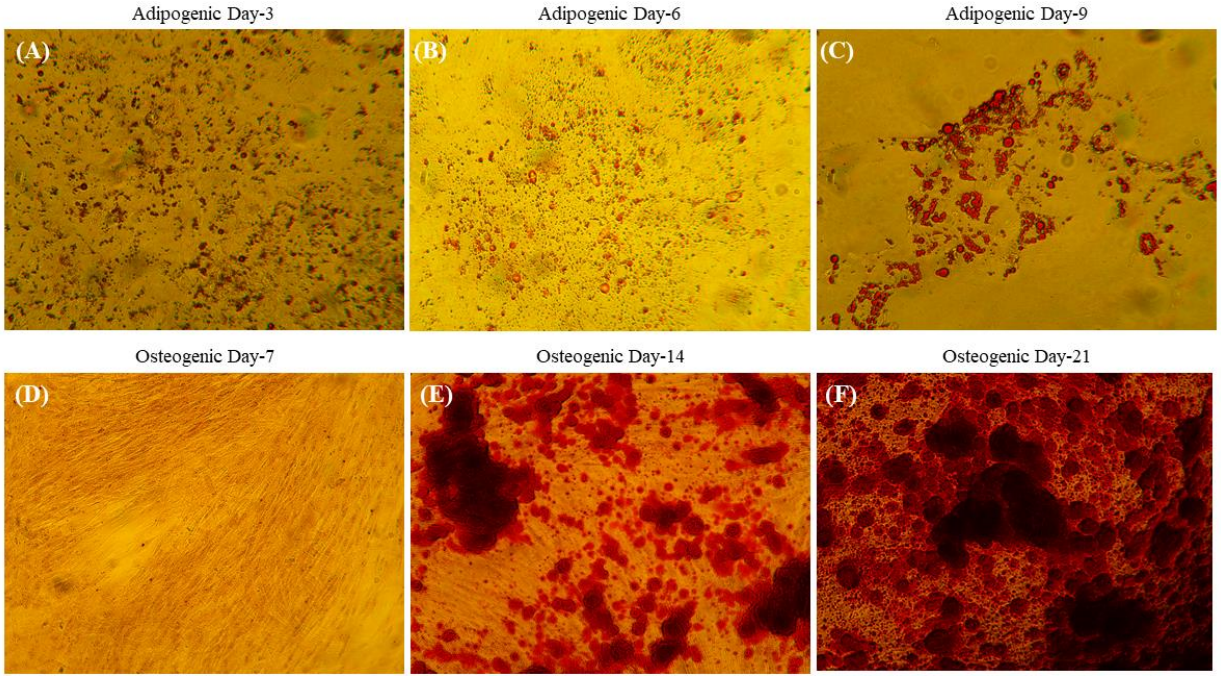

Figure 24: Adipogenic differentiating sample mixed with oil o red + 4% paraformaldehyde and imaged on (A) day-3 (B) day-6 (C) day-9. Osteogenic differentiating sample with alizarin red and 70% ice cold ethanol imaged at (D) day-7 (E) day-14 (F) day-21

Dark field optical imaging and hyperspectral spectroscopy - Our experimental set up consists of a hyperspectral microscope from CytoViva equipped with high intensity halogen light source and a patented nanoscale illumination condenser. The system provides hyperspectral/optical imaging in the visible near-infrared range (400-1000 nm). Spectral data is collected using spectrograph at room temperature with the intensity count being adjusted to a value between 1,000 and 10,000. Each pixel has a spatial area of 25 nm^2 and is exposed for 0.35 seconds in order to capture the entire visible near-infrared spectrum. Light derived from high intensity halogen lamp is projected at oblique angles using the patented condenser in order to obtain fine scattering from all the inter-cellular components with a resolution of ~ 2 nm. Numerical aperture of the condenser lies between 1.2 and 1.4. Dark field optical and hyperspectral images are recorded for three adult human donors after trypsinization of the sample to obtain the best yield at day-3, day-6, and day-9. Difference between optical and hyperspectral images is shown in Figure-25.

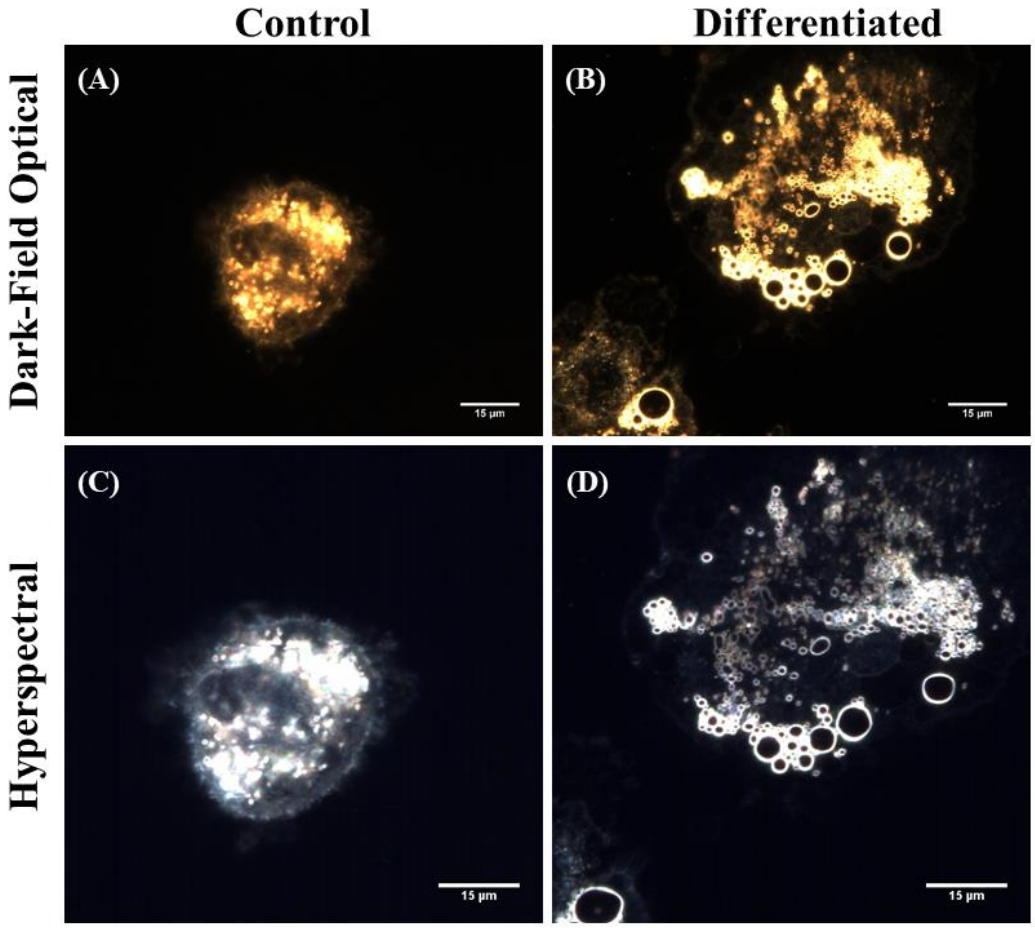

Figure 25: (A) and (B) represent dark-field optical images of control and differentiated cells respectively captured at day-9 of the adipogenic differentiation cell-culture. (C) and (D) represent dark-field hyperspectral images of the control and differentiated cells at day-9 of the adipogenic differentiation

In order to develop spectra based mapping protocol, it is important to have knowledge of the interaction of light with specific scattering chemical/surface constituent. Spectral contribution is different from each cell due to complexity and difference in tissue optics faced by incident light due to membrane and cellular heterogeneity (as shown in Figure-26) due to dissimilar molecular composition. Matrix-assisted laser ionization/desorption (MALDI) is used to identify individual chemical constituents and proteins for the stem-cell sample. By understanding the potential constituents such as peptides, proteins, oligonucleotides, glycopepetides, and phosphopeptides, we can better understand constituent molecules of differentiating and non-differentiating ASCs and develop efficient spectral angle mapping (SAM) algorithms.

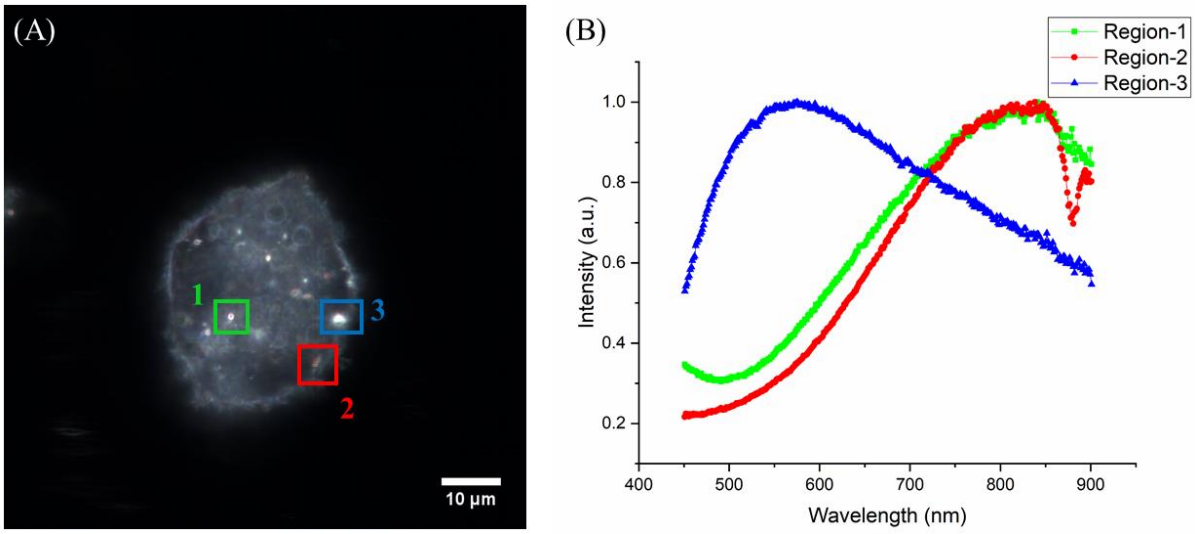

Figure 26: (A) Control ASC marked with three regions of interest on hyperspectral image at 100x in order to collect corresponding spectral signatures (B) Intensity distribution depicting heterogeneous nature of the cell in the VNIR-range from the marked regions in (A)

In this research, three different matrix are used for the optimization. A saturated solution of 2, 5-Dihydroxybenzoic acid (DHB; Sigma-Aldrich, St. Louis, MO, USA) dissolved in a 0.1% trifluoroacetic acid (TFA) in water was used as the matrix. A sample solution of 1 µL was first deposited to the MALDI target plate followed by 1 µL matrix deposition above it and mixing before the drying of the components. MALDI-TOF MS measurements were performed on a commercial instrument (Ultraflextreme, Bruker Daltonics), schematic is shown in Figure-27.

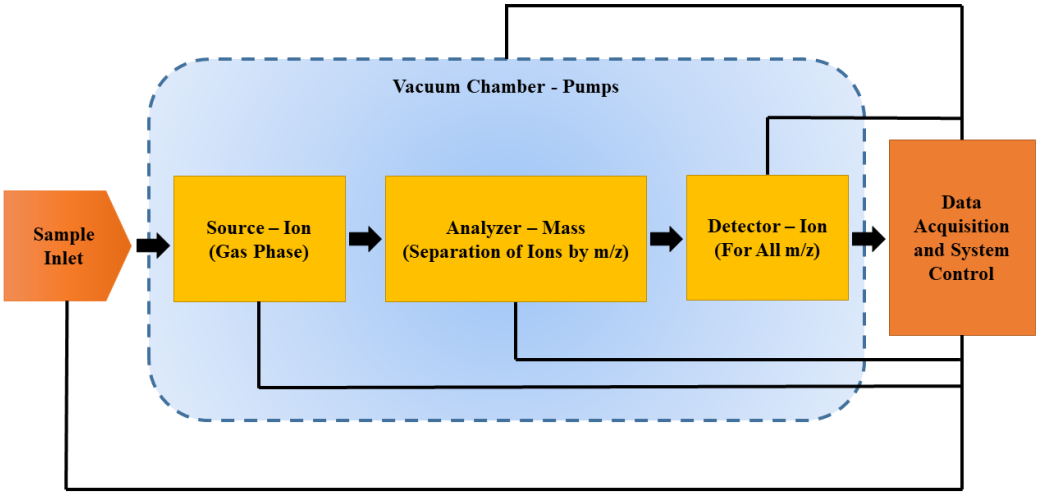

Figure 27: Schematic of MALDI-TOF Mass Spectrometry System

4.4. Results and Discussion

As expected, our investigation of adipogenic stem-cells using dark-field hyperspectral microscope suggest that compared to control (non-differentiated) stem cells, a higher degree of cellular heterogeneity is observed within the differentiated stem-cell populations compared to control biological samples as shown in Figure 28. In particular, we observe the heterogeneous changes within the stem cell morphology due to formation of oil-wells (deposition of fatty acids) during adipogenic differentiation as well as the formation of calcium deposits within ASCs undergoing osteogenesis. Heterogeneity increases with the gain in differentiation time.

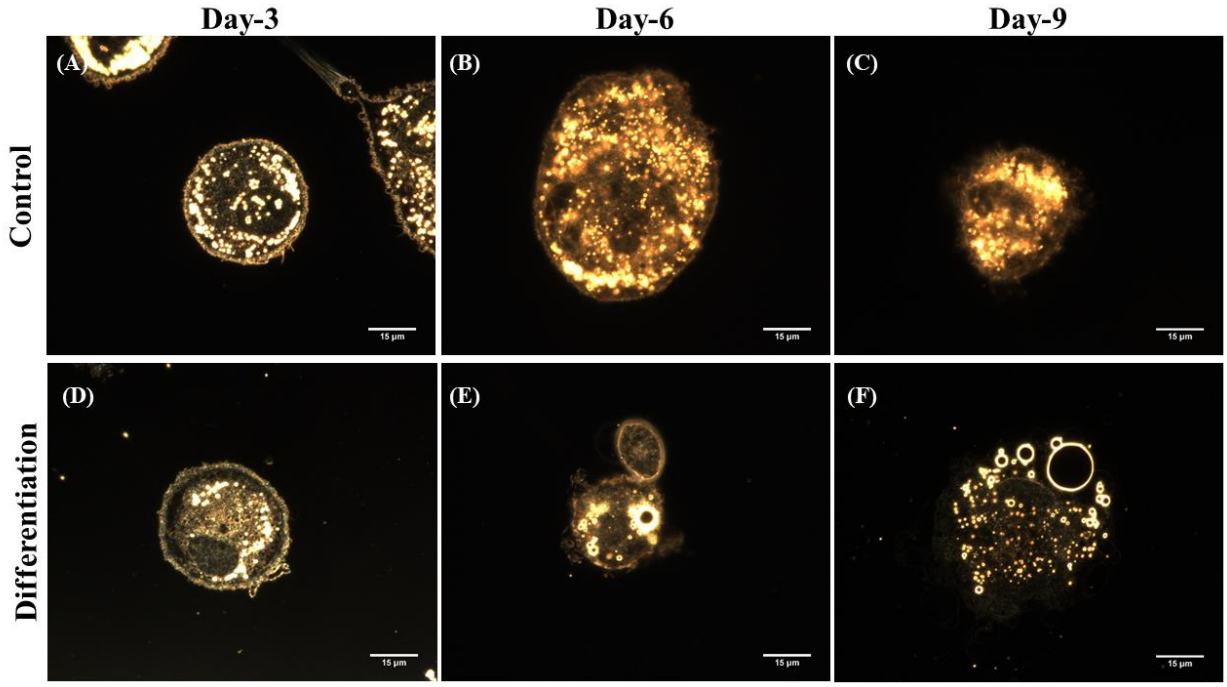

Figure 28: (A), (B), and (C) represent control sample of ASCs imaged at day-3, day-6, and day-9 respectively while (D), (E), (F) represent sample of stem-cells undergoing differentiation due to growth factors induced in stromal media

It is observed that number of oil-wells with varying sizes from 4-8 μm observed at Day-6 increases significantly within the single cells observed at Day-9. Biochemical spectra exhibited from the entire cell and the walls of oil-well is observed to be very distinct from the spectrum exhibited by control stem cells as shown in Figure-29 due to secretion of adiponectin, adipsin, apelin, leptin,

glycerol 3-phosphate dehydrogenase in differentiated adipogenic stem-cell samples. From the Figure-29 we observe no or negligible change in full-width half-maximum of spectra over day-3, day-6, and day-9. Consistent highest intensity peak was observed at 850 nm wavelength.

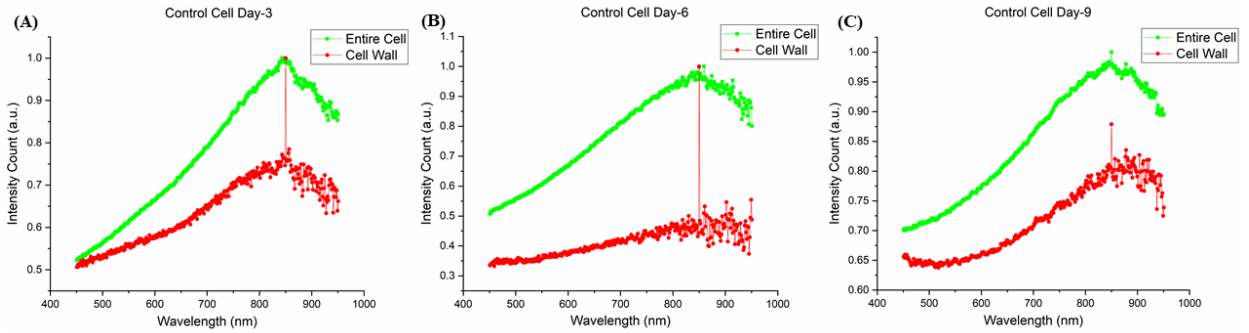

Figure 29: Spectral distribution in VNIR collected from region of interest embedding pixel information of entire adipogenic control cell and from cell wall for (A) day-3, (B) day-6, and (C) day-9

Two very distinct spectral features of the differentiating cells such as peak broadening of full-width half-maximum with gain in cell culture days and blue shifting of the spectra from the wall structures were observed from the intensity distribution over the visible-near infrared region of spectrum as seen in Figure-30. Plots in these figures are the representative spectral distribution of the 25 differentiating cells from the three donors carefully picked and analyzed at day-3, 6 and 9.

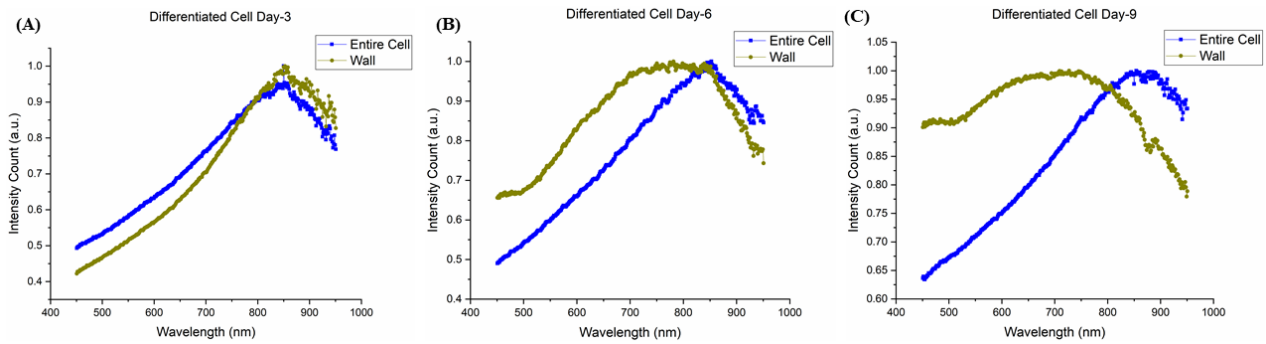

Figure 30: Spectral distribution in VNIR collected from region of interest embedding pixel information of entire differentiated adipogenic cells and from oil-well wall for (A) day-3, (B) day-6, and (C) day-9

We observe variability of hyperspectral signatures and high data redundancy due to significant correlation with the adjacent bands. There is no spectral response from chemical composition close to immersion oil or glycerol while system is not sensitive enough to detect low concentration

molecules. In order to reveal identity of the biological factors being secreted by the cells under all probed different days, mass spectrometry is a good fit for proteomic profiling. Mass spectra of differentiated and control cells from day-9 were recorded in positive ion reflection mode for initial analysis with an accelerating voltage of 25 kilo Volts (kV) from the laser and analyzed in the mass range of 150–5000 Da. The spectra were acquired after calibration of the instrument with a peptide standard (Peptide Calibration Standard II, Bruker Daltonics, MA, USA). Three different matrices were used. A minimum of 500 laser shots per each differentiated as well as control sample was used to generate each mass spectrum as shown in Figure 31.

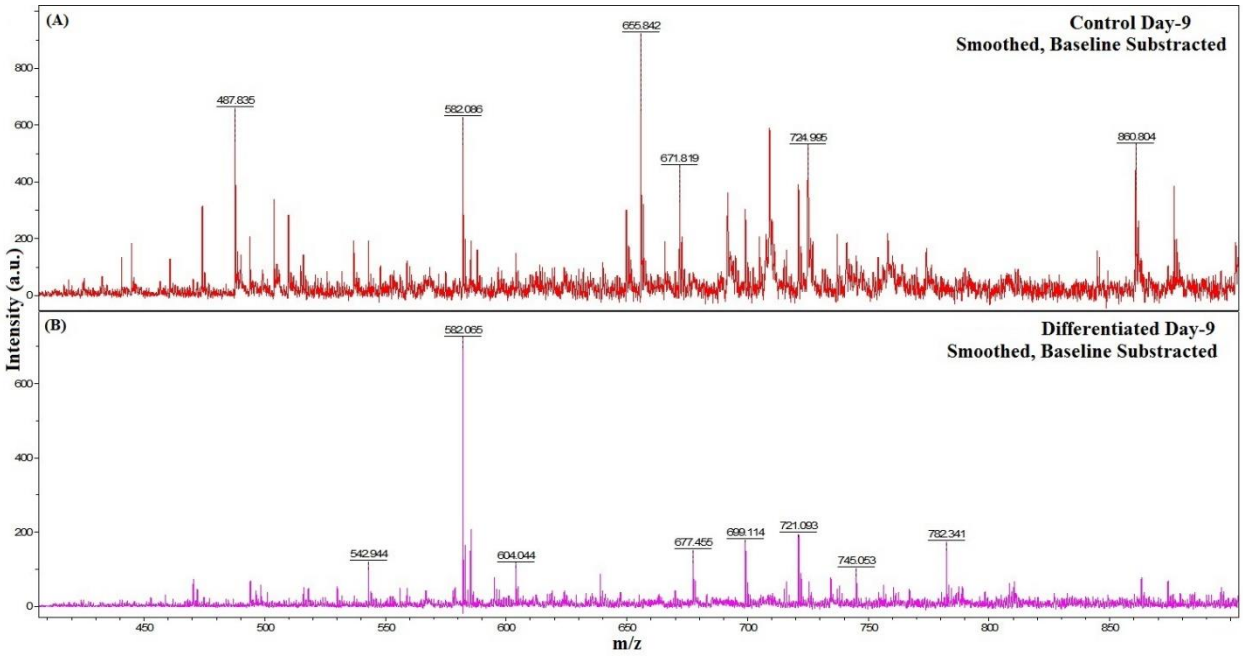

Figure 31: (A) Mass spectrum from control sample of ASCs at day-9 (B) Mass spectrum from differentiated sample of ASCs undergoing adipogenic differentiation imaged at day-9

It was observed that prominent peaks of interest in control sample were observed at 487.835, 582.086, 655.842, 671.819, 724.995, and 860.804 while prominent peaks for differentiation were observed at 542.944, 582.065, 604.044, 677.455, 699.114, 721.093, 745.053, and 782.341. Continuing work includes non-invasive analysis of stem cell osteogenic differentiation process as shown in Figure-32. Mass profiling data is compared with available online proteomic databases to

identify and obtain individual secreted chemicals occurring in differentiated cells. Plan is to record spectrum from this individual chemicals and define the spectral-bands. Mapping of these bands onto control and differentiated cell images can be performed using spectral angle mapping (SAM function). These maps can provide information regarding scattering angle distribution and help identify differentiation rate.

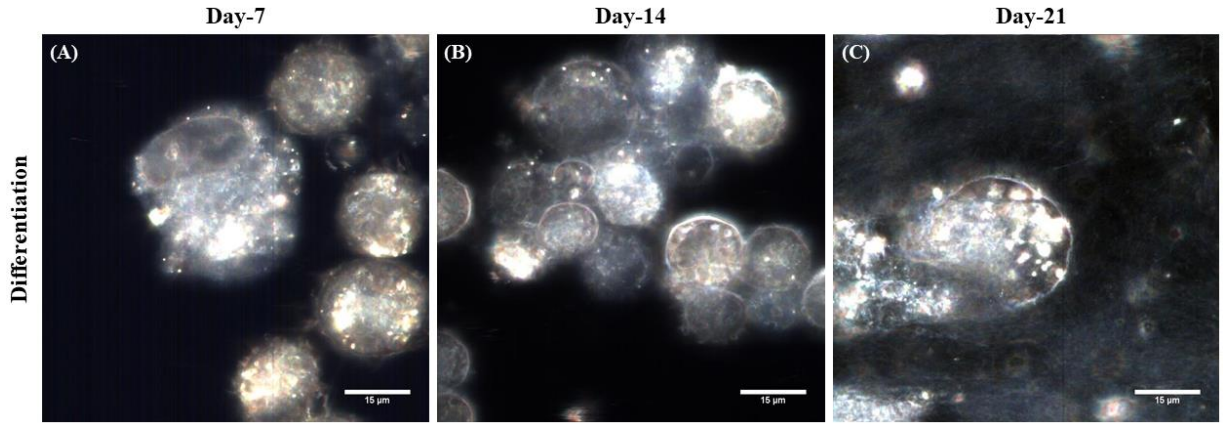

Figure 32: Osteogenic differentiation sample imaged non-invasively at day-7, day-14, and day-21. We observe increase in fusing of the stem-cells and calcium depostion outside of the cellular walls to eventually culture into bone structures

4.5. Future Work

Spectral response of each pixel is stored as a vector. Each vector has dimension value equal to number of wavelengths. And the component of each dimension is corresponding intensity count incident on detector. Inner product of vectors is measured in order to find pixel match as shown in equation [25] where, $I_{P\lambda}$ = pixel vector at point of interest, $I_{R\lambda}$ = reference vector.

$$\theta = \frac{\sum_{\lambda=1}^{n}(I_{P\lambda}I_{R\lambda})}{\sqrt{\sum_{\lambda=1}^{n}(I_{P\lambda})^2}\ \mathrm{X}\ \sqrt{\sum_{\lambda=1}^{n}(I_{R\lambda})^2}}$$

When there is a match between angles confined within corresponding vectors of reference and point of interest, pixels are color mapped and are left uncolored when there is no match as shown in the Figure-33. Cells mapped in this figure are imaged at 100x on day-9 of adipogenic differentiation cell-culture. After acquiring the HSI images, the images are lamp corrected and

spectral libraries are built after defining regions of interest. The library is filtered then against negative control and SAM algorithm is employed to generate chemical maps.

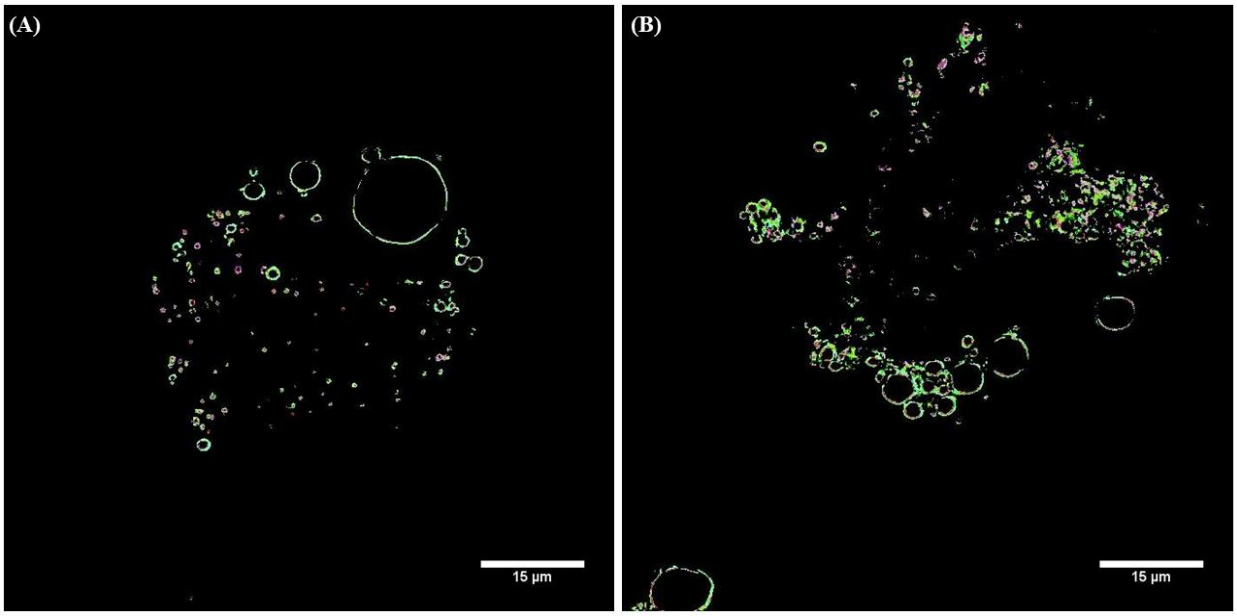

Figure 33: (A) and (B) represent adipogenic differentiated stem cells mapped using reference spectra of unknown chemical detected and recorded at the cell wall of the biological sample

Secondary method to augment processing of the dark-field images of sample non-invasively include developing template match and edge detection algorithms. Statistical study can be performed on the morphology of biological cell and the images can be feed into Matlab. Figure 34 depicts the proposed method.

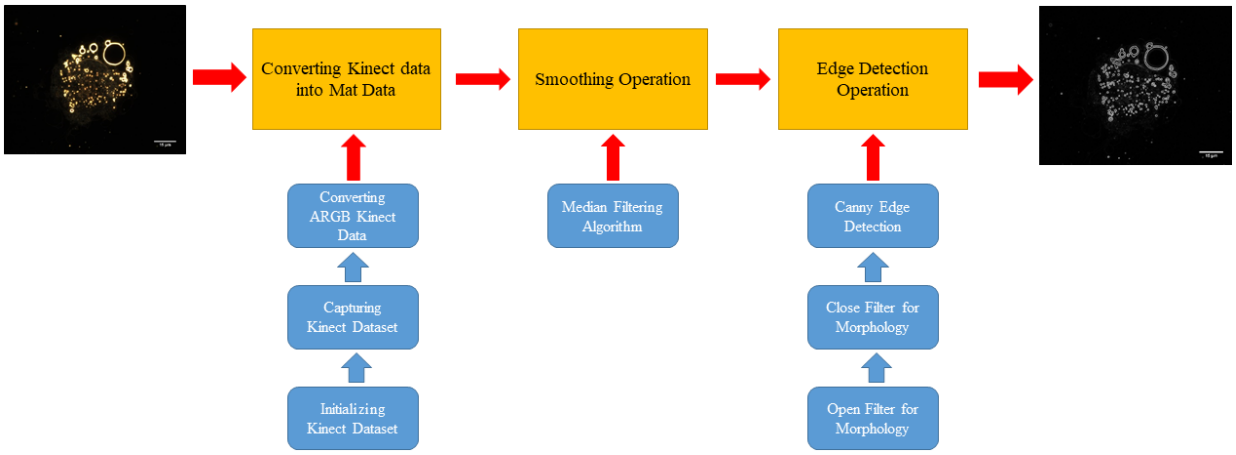

Figure 34: Template match algorithm to analyze dark-field optical images of differentiated stem-cells

Combining spectral angle mapping (SAM) function which includes spectral mapping, with template match algorithms to detect edges on dark-field optical images, we can develop precise and accurate non-invasive protocol to detect single-cell level automated detection of differentiation process.

CHAPTER 5: CONCLUSIONS AND FUTURE PROJECTS

5.1. Conclusions

We have presented a method for large-scale and high throughput characterization of a single nano-particle by combining high resolution nanometer-scale optical imaging technique and hyperspectral spectrometer. Micro-milling and lithography techniques were utilized to cross-correlate optical and electron microscopy technique. Reference libraries for the scattering spectra can provide a high throughput method to perform single particle level polarization dependent microscopy and spectroscopy on large scale. Developing accurate and economic technique to characterize nano-structures will complement high throughput nanofabrication and advanced manufacturing. Also, we have proposed cost efficient and quick characterization of stem-cell differentiation by combing intensity tracking of optical images and mapping of spectral variance based hyperspectral spectrographic data-cubes. In spite of all the progress, practical implementation of a system to control the differentiation of stem cell and maintaining the purity of the isolated cells remains a challenge. There is a need to develop multi-modal imaging modalities which can simultaneously provide functional, morphological and biochemical information of cells, scaffolds as well as extracellular matrix components. Light microscopy and phase contrast microscopy have the advantage of monitoring cells over a large time scale, however, the methods are currently limited by the array of specific chemical information related to cell activity and metabolism they can provide. Hyperspectral microscopy-based imaging is shown to be capable of performing single-cell level analysis. Furthermore, hyperspectral microscopy provides intrinsic imaging contrast due to variations in refractive index and cell thickness, which effects the absorption, reflection, and scattering of light from the cells being investigated. Efforts are being made to combine hyperspectral microscopy with other modalities like FTIR and Raman

spectroscopy to enhance the chemical and material specificity from the imaging data. Other areas of interest include enhancing the resolution and penetration depth of the hyperspectral microscopy to better understand spatial variations within heterogeneous tissues and asymmetric nanostructures.

5.2. Future work

1) When there is increase in aspect ratio, plasmonic resonance wavelengths red-shift to lower energy state. Logical extension of the work mentioned in this thesis is to generate differently oriented nanostructures with similar and precisely calibrated size, shape and thickness of the nano-particle. Popular choice is gold nanorods. Preliminary results include parametric study and mono-directional nanostructures created using e-beam lithography as shown in Figure-35.

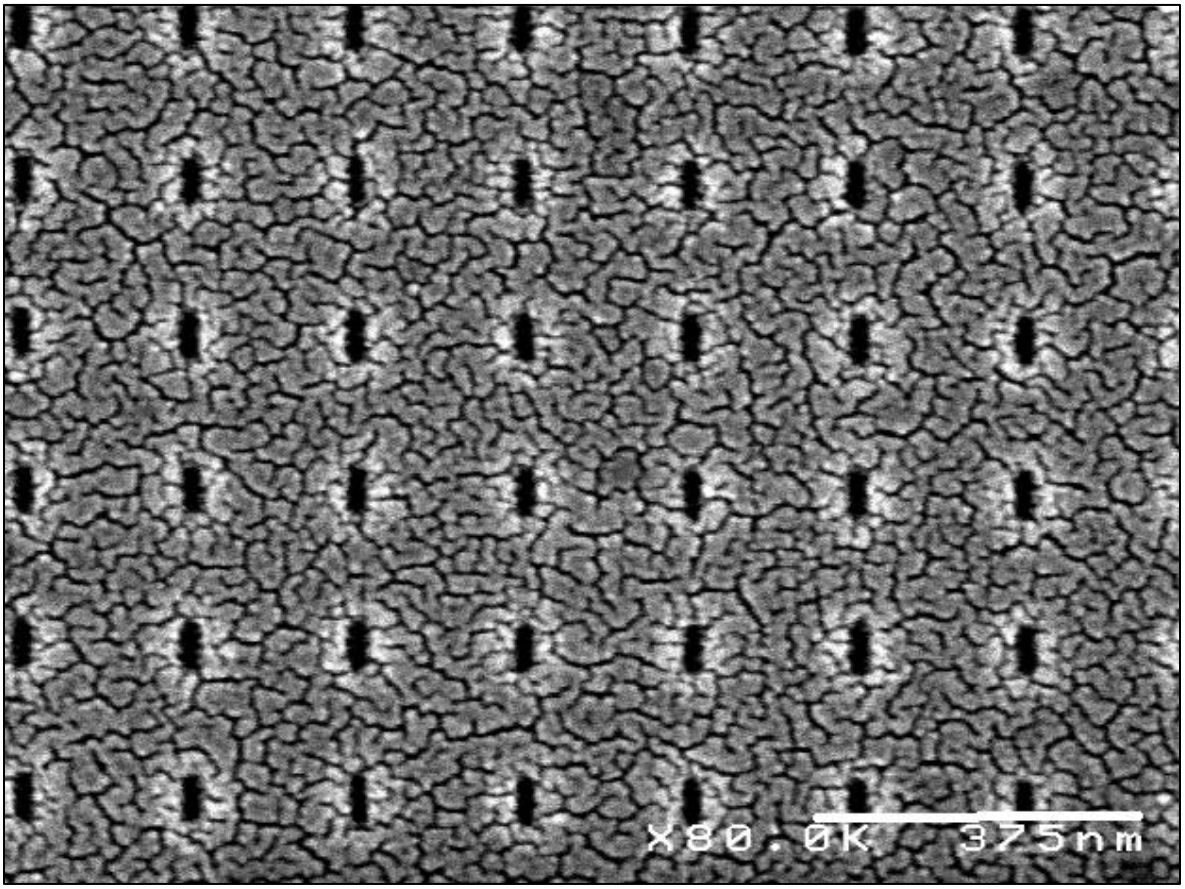

Figure 35: Gold nanorods structures generated using electron beam lithography and oriented at 90 degrees

2) Nano-particles used as a drug delivery or bio sensing probes within biological cellular sample for precise scattering based single-cell quantification and for intra-cellular study. Preliminary data is obtained by embedding gold nanostructures in cells as shown in Figure-36.

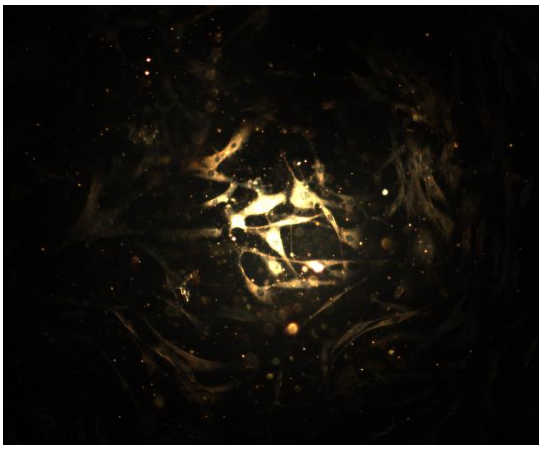

Figure 36: Gold nanostructures infused in human cells and imaged at 10x magnification

CHAPTER 6: LIMITATIONS

Although the HSI systems described above have several advantages over traditional imaging methods, there are some disadvantages and restrictions that are intrinsic to the method. Some of them are:

1) Substantial computing power is required to analyze and collate large amount of spatial and spectral data from the nanoparticles and stem-cells.

2) Constructing the reference spectral libraries can be time-consuming especially in the initial stages of data gathering and analysis. Additionally, it is not always trivial to create reference libraries for *in vitro* and *in vivo* scenarios. For example, since the scattering spectrum of the particle is modified due to changes in its microenvironment such as changes in acidity levels, dissolution characteristics, cluster formation and protein binding, the reference spectral library generated under controlled reference conditions might not be pertinent or relevant to dynamically changing conditions within tissues and cells [21]. Additionally, the deconvolution and/or construction of characteristic spectra for complex systems will require the development of specific and unique control systems. This inability to construct specific and unique control systems will severely limit the generation and realization of standard, universally applicable reference libraries [24]. It requires prolonged exposure time and therefore it is beset by continuous motion from the specimen. In vivo studies become difficult. Rapid movements of the shifting artifacts affect pixel scanning and linear scanning instruments. This generates laborious image analysis and processing after the experiment or diagnosis. High intensity of light sometimes damages the original morphology of the biomolecule.

3) HSI is slower than simple dark field imaging. However, HSI is still less cumbersome and rapid in comparison to corresponding sample preparation time and analysis by standard imaging

methods like electron microscopy. Finally, HSI does generate lower resolution images than scanning probe microscopy-based techniques (such as the atomic force microscopy, AFM or electron-microscopy) and electron microscopy based techniques (such as transmission electron microscopy, TEM). AFM and TEM are capable of resolving individual atoms, whereas the resolution of HSI is typically limited to ~200 nm; although HSI can theoretically detect 10 nm individual particles [7].

4) Image formation is only two-dimensional compared to 3 –dimensional view. Therefore we face high difficulty in probing abnormalities which can only be probed by appreciating depth. Because vital spectral wavelengths and spatial information might be affected or lost for which user might not be aware about the same.

5) Hyperspectral imaging system is not portable. Due to bulk optics and complex setup, HSI system is mostly benchtop.

REFERENCES

1. Stender, A.S., et al., *Single cell optical imaging and spectroscopy.* Chemical reviews, 2013. **113**(4): p. 2469-2527.

2. Hell, S.W., *Far-field optical nanoscopy.* science, 2007. **316**(5828): p. 1153-1158.

3. Hickey, W.J., et al., *Three-dimensional bright-field scanning transmission electron microscopy elucidate novel nanostructure in microbial biofilms.* Journal of microscopy, 2017. **265**(1): p. 3-10.

4. Mock, J., et al., *Shape effects in plasmon resonance of individual colloidal silver nanoparticles.* The Journal of Chemical Physics, 2002. **116**(15): p. 6755-6759.

5. Zheng, W., et al., *Cryo-EM of the Bacteriophage Tail Tube at Better than 3.5 Å Resolution.* Biophysical Journal, 2017. **112**(3): p. 573a-574a.

6. Crawford, R., et al., *Analysis of lipid nanoparticles by Cryo-EM for characterizing siRNA delivery vehicles.* International journal of pharmaceutics, 2011. **403**(1-2): p. 237-244.

7. Galler, K., et al., *Making a big thing of a small cell–recent advances in single cell analysis.* Analyst, 2014. **139**(6): p. 1237-1273.

8. Junno, T., et al., *Controlled manipulation of nanoparticles with an atomic force microscope.* Applied Physics Letters, 1995. **66**(26): p. 3627-3629.

9. Seidman, D.N., *Three-dimensional atom-probe tomography: Advances and applications.* Annu. Rev. Mater. Res., 2007. **37**: p. 127-158.

10. Devaraj, A., et al., *Understanding atom probe tomography of oxide-supported metal nanoparticles by correlation with atomic-resolution electron microscopy and field evaporation simulation.* The journal of physical chemistry letters, 2014. **5**(8): p. 1361-1367.

11. Kherlopian, A.R., et al., *A review of imaging techniques for systems biology.* BMC systems biology, 2008. **2**(1): p. 74.

12. Choi, J.s., et al., *A hybrid nanoparticle probe for dual-modality positron emission tomography and magnetic resonance imaging.* Angewandte Chemie International Edition, 2008. **47**(33): p. 6259-6262.

13. Amemiya, S., et al., *Scanning electrochemical microscopy.* Annu. Rev. Anal. Chem., 2008. **1**: p. 95-131.

14. Zhu, Y., et al., *Synchrotron-based X-ray microscopy for sub-100 nm resolution cell imaging.* Current opinion in chemical biology, 2017. **39**: p. 11-16.

15. Rabin, O., et al., *An X-ray computed tomography imaging agent based on long-circulating bismuth sulphide nanoparticles.* Nature materials, 2006. **5**(2): p. 118.

16. Downes, A., et al., *Raman spectroscopy and CARS microscopy of stem cells and their derivatives.* Journal of Raman Spectroscopy, 2011. **42**(10): p. 1864-1870.

17. Nie, S. and S.R. Emory, *Probing single molecules and single nanoparticles by surface-enhanced Raman scattering.* science, 1997. **275**(5303): p. 1102-1106.

18. O'Neal, D.P., et al., *Photo-thermal tumor ablation in mice using near infrared-absorbing nanoparticles.* Cancer letters, 2004. **209**(2): p. 171-176.

19. Gerber, H.-P., et al., *VEGF regulates haematopoietic stem cell survival by an internal autocrine loop mechanism.* Nature, 2002. **417**(6892): p. 954.

20. Cunningham, C.H., et al., *Positive contrast magnetic resonance imaging of cells labeled with magnetic nanoparticles.* Magnetic Resonance in Medicine, 2005. **53**(5): p. 999-1005.

21. Roth, G.A., et al., *Hyperspectral microscopy as an analytical tool for nanomaterials.* Wiley Interdisciplinary Reviews: Nanomedicine and Nanobiotechnology, 2015. **7**(4): p. 565-579.

22. Schultz, R.A., et al., *Hyperspectral imaging: a novel approach for microscopic analysis.* Cytometry Part A, 2001. **43**(4): p. 239-247.

23. Wang, X., Y. Cui, and J. Irudayaraj, *Single-cell quantification of cytosine modifications by hyperspectral dark-field imaging.* ACS nano, 2015. **9**(12): p. 11924-11932.

24. Conti, M., et al., *Building up spectral libraries for mapping erythrocytes by hyperspectral dark field microscopy.* Biomedical Spectroscopy and Imaging, 2016. **5**(2): p. 175-184.

25. More, S.S. and R. Vince, *Hyperspectral imaging signatures detect amyloidopathy in Alzheimer's mouse retina well before onset of cognitive decline.* ACS chemical neuroscience, 2014. **6**(2): p. 306-315.

26. Lu, G. and B. Fei, *Medical hyperspectral imaging: a review.* Journal of biomedical optics, 2014. **19**(1): p. 010901.

27. Vo-Dinh, T., *A hyperspectral imaging system for in vivo optical diagnostics.* IEEE Engineering in Medicine and Biology Magazine, 2004. **23**(5): p. 40-49.

28. Oh, E.S., et al., *Hyperspectral fluorescence imaging for cellular iron mapping in the in vitro model of Parkinson's disease.* Journal of Biomedical Optics, 2013. **19**(5): p. 051207.

29. Mehta, N., et al., *Single-Cell Analysis Using Hyperspectral Imaging Modalities.* Journal of biomechanical engineering, 2018. **140**(2): p. 020802.

30. Maier, S.A., et al., *Local detection of electromagnetic energy transport below the diffraction limit in metal nanoparticle plasmon waveguides.* Nature materials, 2003. **2**(4): p. 229.

31. Lanza, G.M., et al., *Targeted antiproliferative drug delivery to vascular smooth muscle cells with a magnetic resonance imaging nanoparticle contrast agent: implications for rational therapy of restenosis.* Circulation, 2002. **106**(22): p. 2842-2847.

32. Willets, K.A. and R.P. Van Duyne, *Localized surface plasmon resonance spectroscopy and sensing.* Annu. Rev. Phys. Chem., 2007. **58**: p. 267-297.

33. Kawata, S., Y. Inouye, and P. Verma, *Plasmonics for near-field nano-imaging and superlensing.* Nature Photonics, 2009. **3**(7): p. 388.

34. Rechberger, W., et al., *Optical properties of two interacting gold nanoparticles.* Optics communications, 2003. **220**(1-3): p. 137-141.

35. Barnes, W.L., A. Dereux, and T.W. Ebbesen, *Surface plasmon subwavelength optics.* nature, 2003. **424**(6950): p. 824.

36. Ye, X., et al., *Morphologically controlled synthesis of colloidal upconversion nanophosphors and their shape-directed self-assembly.* Proceedings of the National Academy of Sciences, 2010. **107**(52): p. 22430-22435.

37. Murray, W. and W. Barnes, *Adv. Mater.(Weinheim, Ger.).* 2007.

38. Olson, J., et al., *Optical characterization of single plasmonic nanoparticles.* Chemical Society Reviews, 2015. **44**(1): p. 40-57.

39. Brown, L.V., et al., *Heterodimers: plasmonic properties of mismatched nanoparticle pairs.* ACS nano, 2010. **4**(2): p. 819-832.

40. Grag, P.; Available from: https://upload.wikimedia.org/wikipedia/commons/4/4f/PSC_using_Metal_Nanoparticles.png.

41. Labion.

42. Group, T.J.

43. Chang, W.-S., et al., *Plasmonic nanorod absorbers as orientation sensors.* Proceedings of the National Academy of Sciences, 2010. **107**(7): p. 2781-2786.

44. Tabor, C., D. Van Haute, and M.A. El-Sayed, *Effect of orientation on plasmonic coupling between gold nanorods.* Acs Nano, 2009. **3**(11): p. 3670-3678.

45. Kelly, K.L., et al., *The optical properties of metal nanoparticles: the influence of size, shape, and dielectric environment*. 2003, ACS Publications.

46. Encina, E.R. and E.A. Coronado, *Plasmon coupling in silver nanosphere pairs.* The Journal of Physical Chemistry C, 2010. **114**(9): p. 3918-3923.

47. Zhang, P., et al., *Super-resolution of fluorescence-free plasmonic nanoparticles using enhanced dark-field illumination based on wavelength-modulation.* Scientific reports, 2015. **5**: p. 11447.

48. Zhang, Z., et al., *Controlled inkjetting of a conductive pattern of silver nanoparticles based on the coffee-ring effect.* Advanced Materials, 2013. **25**(46): p. 6714-6718.

49. Choi, S., et al., *Coffee-ring effect-based three dimensional patterning of micro/nanoparticle assembly with a single droplet.* Langmuir, 2010. **26**(14): p. 11690-11698.

50. Mehta, N., et al. *Orientational imaging of a single plasmonic nanoparticle using dark-field hyperspectral imaging*. in *Plasmonics: Design, Materials, Fabrication, Characterization, and Applications XV*. 2017. International Society for Optics and Photonics.

51. Monk, P., *Finite element methods for Maxwell's equations*. 2003: Oxford University Press.

52. Weast, R.C., M.J. Astle, and W.H. Beyer, *CRC handbook of chemistry and physics*. Vol. 1990. 1989: CRC press, Boca raton FL.

53. incurebles, U.-C.t.; Available from: http://rejuvaa.com/StemCellResearch/AdiposeStemCells.

54. Seng, P., et al., *Ongoing revolution in bacteriology: routine identification of bacteria by matrix-assisted laser desorption ionization time-of-flight mass spectrometry.* Clinical Infectious Diseases, 2009. **49**(4): p. 543-551.

55. Kim, A. and B.C. Wilson, *Measurement of ex vivo and in vivo tissue optical properties: methods and theories*, in *Optical-Thermal Response of Laser-Irradiated Tissue*. 2010, Springer. p. 267-319.

56. Sandell, J.L. and T.C. Zhu, *A review of in-vivo optical properties of human tissues and its impact on PDT.* Journal of biophotonics, 2011. **4**(11-12): p. 773-787.

57. Bashkatov, A.N., E.A. Genina, and V.V. Tuchin, *Optical properties of skin, subcutaneous, and muscle tissues: a review.* Journal of Innovative Optical Health Sciences, 2011. **4**(01): p. 9-38.

58. Jacques, S.L., *Optical properties of biological tissues: a review.* Physics in Medicine & Biology, 2013. **58**(11): p. R37.

59. Luu, Y.K., et al., *Mechanical stimulation of mesenchymal stem cell proliferation and differentiation promotes osteogenesis while preventing dietary-induced obesity.* Journal of Bone and Mineral Research, 2009. **24**(1): p. 50-61.

60. Peterson, S.M. and J.L. Freeman, *RNA isolation from embryonic zebrafish and cDNA synthesis for gene expression analysis.* Journal of visualized experiments: JoVE, 2009(30).

61. Vermaas, W.F., et al., *In vivo hyperspectral confocal fluorescence imaging to determine pigment localization and distribution in cyanobacterial cells.* Proceedings of the National Academy of Sciences, 2008. **105**(10): p. 4050-4055.

62. Haaland, D.M. and E.V. Thomas, *Partial least-squares methods for spectral analyses. 1. Relation to other quantitative calibration methods and the extraction of qualitative information.* Analytical chemistry, 1988. **60**(11): p. 1193-1202.

63. Ruckebusch, C. and L. Blanchet, *Multivariate curve resolution: a review of advanced and tailored applications and challenges.* Analytica chimica acta, 2013. **765**: p. 28-36.

64. Wang, W., et al., *Single cells and intracellular processes studied by a plasmonic-based electrochemical impedance microscopy.* Nature chemistry, 2011. **3**(3): p. 249.

65. Wood, R.W., *XLII. On a remarkable case of uneven distribution of light in a diffraction grating spectrum.* The London, Edinburgh, and Dublin Philosophical Magazine and Journal of Science, 1902. **4**(21): p. 396-402.

66. Otto, A., *Excitation of nonradiative surface plasma waves in silver by the method of frustrated total reflection.* Zeitschrift für Physik A Hadrons and nuclei, 1968. **216**(4): p. 398-410.

67. Kretschmann, E. and H. Raether, *Radiative decay of non radiative surface plasmons excited by light.* Zeitschrift für Naturforschung A, 1968. **23**(12): p. 2135-2136.

68. Chu, X. and S.-I. Chu, *Time-dependent density-functional theory for molecular processes in strong fields: Study of multiphoton processes and dynamical response of individual valence electrons of N 2 in intense laser fields.* Physical Review A, 2001. **64**(6): p. 063404.

69. Wang, W., et al., *Mapping single-cell–substrate interactions by surface plasmon resonance microscopy.* Langmuir, 2012. **28**(37): p. 13373-13379.

70. Berguiga, L., et al., *Time-lapse scanning surface plasmon microscopy of living adherent cells with a radially polarized beam.* Applied optics, 2016. **55**(6): p. 1216-1227.

71. Homola, J., *Surface plasmon resonance sensors for detection of chemical and biological species.* Chemical reviews, 2008. **108**(2): p. 462-493.

72. Chattopadhyay, P.K., et al., *Single-cell technologies for monitoring immune systems.* Nature immunology, 2014. **15**(2): p. 128.

73. Laplatine, L., et al., *Spatial resolution in prism-based surface plasmon resonance microscopy.* Optics Express, 2014. **22**(19): p. 22771-22785.

74. Fu, D., W. Yang, and X.S. Xie, *Label-free imaging of neurotransmitter acetylcholine at neuromuscular junctions with stimulated Raman scattering.* Journal of the American Chemical Society, 2016. **139**(2): p. 583-586.

75. Chaudhari, K. and T. Pradeep, *Spatiotemporal mapping of three dimensional rotational dynamics of single ultrasmall gold nanorods.* Scientific reports, 2014. **4**: p. 5948.

76. Verebes, G.S., et al., *Hyperspectral enhanced dark field microscopy for imaging blood cells.* Journal of biophotonics, 2013. **6**(11-12): p. 960-967.

77. Mortimer, M., A. Kahru, and V.I. Slaveykova, *Uptake, localization and clearance of quantum dots in ciliated protozoa Tetrahymena thermophila.* Environmental pollution, 2014. **190**: p. 58-64.

78. Misra, S.K., et al., *Hyperspectral Imaging Offers Visual and Quantitative Evidence of Drug Release From Zwitterionic-Phospholipid-Nanocarbon When Concurrently Tracked in 3D Intracellular Space.* Advanced Functional Materials, 2016. **26**(44): p. 8031-8041.

79. Gosnell, M.E., et al., *Quantitative non-invasive cell characterisation and discrimination based on multispectral autofluorescence features.* Scientific reports, 2016. **6**: p. 23453.

80. Khaodhiar, L., et al., *The use of medical hyperspectral technology to evaluate microcirculatory changes in diabetic foot ulcers and to predict clinical outcomes.* Diabetes care, 2007. **30**(4): p. 903-910.

81. Liu, L. and M. Ngadi, *Detecting fertility and early embryo development of chicken eggs using near-infrared hyperspectral imaging.* Food and Bioprocess Technology, 2013. **6**(9): p. 2503-2513.

82. Bohren, C.F. and D.R. Huffman, *Absorption and scattering by a sphere*. 1983: Wiley Online Library.

APPENDIX A: HYPERSPECTRAL IMAGING SYSTEM

Traditionally, the following spectral ranges have been defined for various imaging techniques: ultraviolet (200 to 400 nm), visible (400 to 780 nm), near-infrared (780 to 2500 nm) and mid-infrared (2500 to 25,000 nm); there are some of the major differences between various imaging modalities: monochrome, RGB, spectroscopy, multispectral, and hyperspectral imaging. Monochrome collects light interacting with a sample at a single wavelength, RGB at three distinct wavelengths (red, green and blue) as well as information on the location (spatial) from which the light is being collected while spectroscopy allows a full range of wavelengths to be collected but not the location, while multispectral imaging or hyperspectral imaging (HSI) allows a full range of wavelengths to be collected as well as location information [26]. However, multispectral imaging has a spectral resolution greater than 10 nm and the number of spectral bands are limited from three to ten spaced bands while commercially available HIS systems have a finer resolution (< 5 nm) with spectral bands numbering from tens to hundreds in a continuous range. The differences between HSI and RGB which depicts light reflectance curve of a single pixel from an arbitrary sample imaged using both these methods. The hyperspectral image contains information in a continuous visible-near infrared spectrum compared to the intensity curve from RGB imaging that provides data centered at only three prominent wavelengths. The additional spectral information contained with the continuous hyperspectral image can be utilized to more accurately analyze and understand micro- and nano-scale features that are not feasible using the discrete RGB imaging dataset [26].

Table 3 provides a summary of the current commercially available HSI systems. Briefly, spectral resolution below 1 nm can be achieved using hyperspectral imaging systems from P&P Optica, Photon Etc., Gooch & and PARISS. Other commercially available HSI systems include Montana

based Resonon and Alabama based CytoViva both of whom offer resolution of ~2 nm while the San Diego based Surface Optics Corporation has a lower resolution of ~4 nm.

Table A.1: A Summary of the Current Commercially Available HIS systems

Commercially Available Hyperspectral Imaging Systems	Spectral Resolution	Illumination Source for the HSI	Spectral Range	Software	Origin
Bayspec	<5 nm	-	600-1000 nm	ENVI	California, USA
CytoViva	2.0 nm	High Intensity Halogen	400-1000 nm	ENVI	Alabama, USA
Gooch & Housego	0.6 nm	Halogen	400-1000 nm	μ-Manager	Ilminster, United Kingdom
Norsk Elektro Optikk	3.7 nm	LED	400-2500 nm	-	Skedsmokorset, Norway
PARISS	1 nm	Application Based	365-920 nm	PARISS	USA
P&P Optica	0.1 nm	Halogen	350-2500 nm	PPO IRIS	Ontario, Canada
Photon Etc.	0.2 nm	Tunable Laser	400-1000 nm	PHySpec	Montreal, Canada
Resonon	2.1 nm	Halogen	350-1700 nm	Spectronon Pro	Montana, USA
SPECIM	2.8 nm	Application Based	400-1000 nm	SpecSensor SDK	Oulu, Finland
Surface Optics Corporation	4.68 nm	Halogen	400-1000 nm	SRAnalysis	California, USA

Irrespective of the resolution of these systems, all of these systems are capable of assessing subcellular components (at sub-micron scales). Thus, there is no relative advantage or

disadvantage between these systems for single cell analysis. However, P&P Optica offers wider spectral range from 350-2500 nm (i.e. the spectrum of visible and near-infrared) while the other three systems have a range within visible and some part of near-infrared region (i.e. between 360-1000 nm). Although it should be noted that the spectral range of those system can be increased by changing the Si-based detector to InGaAs detectors for the short-wave infra-red (SWIR) regions. The wider spectral range should theoretically enable more information to be gleaned from the system but the accompanying complexity in data analysis should also be noted. The light source used in the system from Photon Etc. is a laser compared to halogen light sources offered in most other systems. Norway headquartered Norsk Elekto Optikk offers relatively different illumination mode consisting of a light emitting diode source. CytoViva hyperspectral imaging system is comparatively newer and has been most widely used in recent research studies [21]. The relative advantages and disadvantages of these systems are dependent on the choice of specific applications as well as the availability of references libraries for data analysis. All of which can affect the overall cost of the system.

Hyperspectral imagers either use the point imaging modality or slit imaging modality. Image capturing methods include time-based scanning of the two dimensional scene pixel-by-pixel using various types of spectrometers such as Fourier transform spectrometer, spectra-dependent time based, Hadamard transform slit spectrometers or use bandpass filters to capture the image in spectral bandwidths. Filter based method is less robust and include opto-acoustic tuning filters or liquid-crystal based spectral filtering. Recently holographic imaging volume-based methods have been used in practice.

APPENDIX B: PROPERTIES OF PLASMONIC NANOSTRUCTURES

When the electromagnetic radiation is incident on the plasmonic nanostructure, incoming photons are either absorbed or scattered. In order to find the analytical solution to scattering and absorption components of the light incident on nanoparticle, Mie theory is used to solve Maxwell's equations for quasi-static condition. Here we have directly taken into account electric field in z-direction and incoming at the cross-section [38],

$$E_{extinction} = E_o - \left[\frac{\epsilon_{in} - \epsilon_{out}}{\epsilon_{in} + 2\epsilon_{out}}\right] R^3 E_o \left[\frac{1}{r^3} - \frac{3z}{r^5}(x + y + z)\right]$$

$$S_{Scattering} = \frac{W_{Scattering}}{I_{img}}$$

$$S_{extinction} = \frac{W_{extinction}}{I_{img}}$$

Particle of radius R, dielectric function is given by $\epsilon_{nanoparticle} = \epsilon_{real} + i\epsilon_{img}$ and for the medium is ϵ_n. Expression for scattering and extinction cross-section [82]are given as follow:

$$S_{Scattering} = \frac{\lambda_o^2 R^2}{2\pi\epsilon_o} \sum_{k=1}^{\infty} (2k+1)\{|a_k^2| + |b_k^2|\}$$

$$S_{extinction} = \frac{\lambda_o^2 R^2}{2\pi\epsilon_o} \sum_{k=1}^{\infty} (2k+1)\, Re\,[a_k + b_k]$$

Here modes can vary from k=1 (single mode), k=2 (quadrupole mode) to higher order multi-modes. To simplify the solutions, we introduce Bessel function coefficients to solve for a_k and b_k.

$$a_k = \frac{m\varphi_k(my)\varphi_k'(y) - \varphi_k(y)\varphi_k'(my)}{m\varphi_k(my)\xi_k'(y) - \xi_k(y)\varphi_k'(my)}$$

$$b_k = \frac{\varphi_k(my)\varphi_k'(y) - m\varphi_k(y)\varphi_k'(my)}{\varphi_k(my)\xi_k'(y) - m\xi_k(y)\varphi_k'(my)}$$

Here, $y = \frac{2\pi\sqrt{\epsilon_n}}{\lambda_o}$

$$\varphi_k(y) = \left(\frac{\pi y}{2}\right)^{\frac{1}{2}} J_{k+\frac{1}{2}}(y)$$

$$\xi_k(y) = \left(\frac{\pi y}{2}\right)^{\frac{1}{2}} [J_{k+\frac{1}{2}}(y) + iY_{k+\frac{1}{2}}(y)]$$

Here J_k and Y_k are the power series expansion terms of the Bessel functions for structures which are spherical in shape.

APPENDIX C: LETTERS OF PERMISSION

1) Permission for Mehta N, Shaik S, Devireddy R, and Gartia M. Single-Cell Analysis Using Hyperspectral Imaging Modalities. ASME. J Biomech Eng. 2018; 140(2):020802-020802-16. doi:10.1115/1.4038638

AMERICAN SOCIETY OF MECHANICAL ENGINEERS ASME ORDER DETAILS

Apr 08, 2018

Order Number	501385975
Order date	Apr 07, 2018
Licensed content publisher	American Society of Mechanical Engineers ASME
Licensed content title	Journal of biomechanical engineering
Licensed content date	Jan 1, 1977
Type of Use	Thesis/Dissertation
Requestor type	Author of requested content
Format	Print
Portion	chapter/article
The requesting person/organization is:	Nishir Mehta
Title or numeric reference of the portion(s)	Chapter 1, Chapter 2, Chapter 3, Chapter 5
Title of the article or chapter the portion is from	N/A
Editor of portion(s)	N/A
Author of portion(s)	Nishir Mehta
Volume of serial or monograph.	N/A
Issue, if republishing an article from a serial	N/A
Page range of the portion	
Publication date of portion	5/11/2018
Rights for	Main product
Duration of use	Current edition and up to 5 years
Creation of copies for the disabled	no
With minor editing privileges	yes
For distribution to	United States
In the following language(s)	Original language of publication
With incidental promotional use	no
The lifetime unit quantity of new product	Up to 499
Title	Hyperspectral Imaging for Characterizing Single Plasmonic Nanostructure and Single-Cell Analysis
Instructor name	Manas Ranjan Gartia
Institution name	Louisiana State University
Expected presentation date	May 2018
Total (may include CCC user fee)	Not Available

Figure C.1: Permission from ASME Journal of Biomechanical Engineering

2) Permission for Nishir Mehta, Amirreza Mahigir, Georgios Veronis, Manas Ranjan Gartia, "Orientational imaging of a single plasmonic nanoparticle using dark-field hyperspectral imaging," Proc. SPIE 10346, Plasmonics: Design, Materials, Fabrication, Characterization, and Applications XV, 1034631 (25 August 2017); doi: 10.1117/12.2274695; https://doi.org/10.1117/12.2274695.

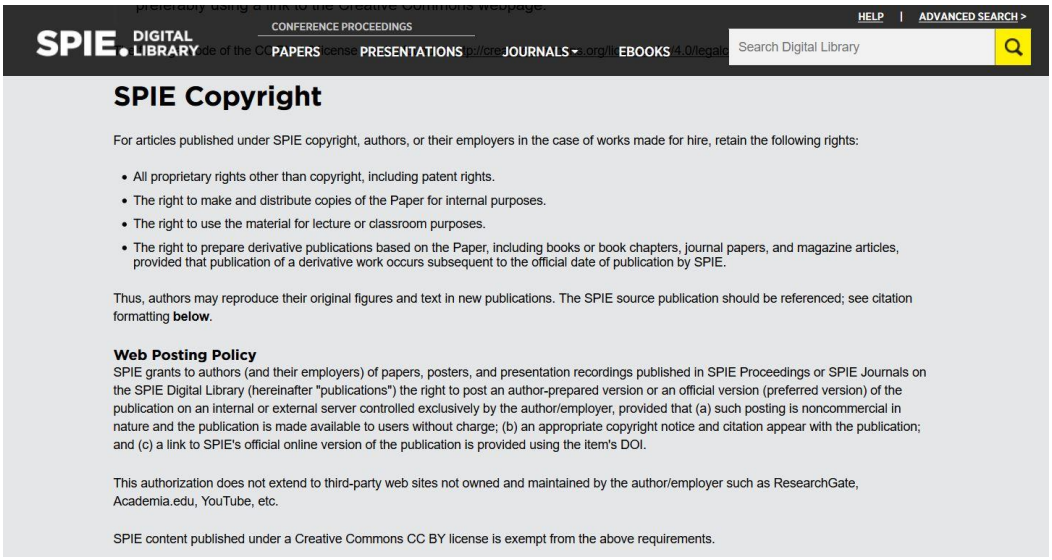

Figure C.2: Copyright rules from SPIE Digital Library

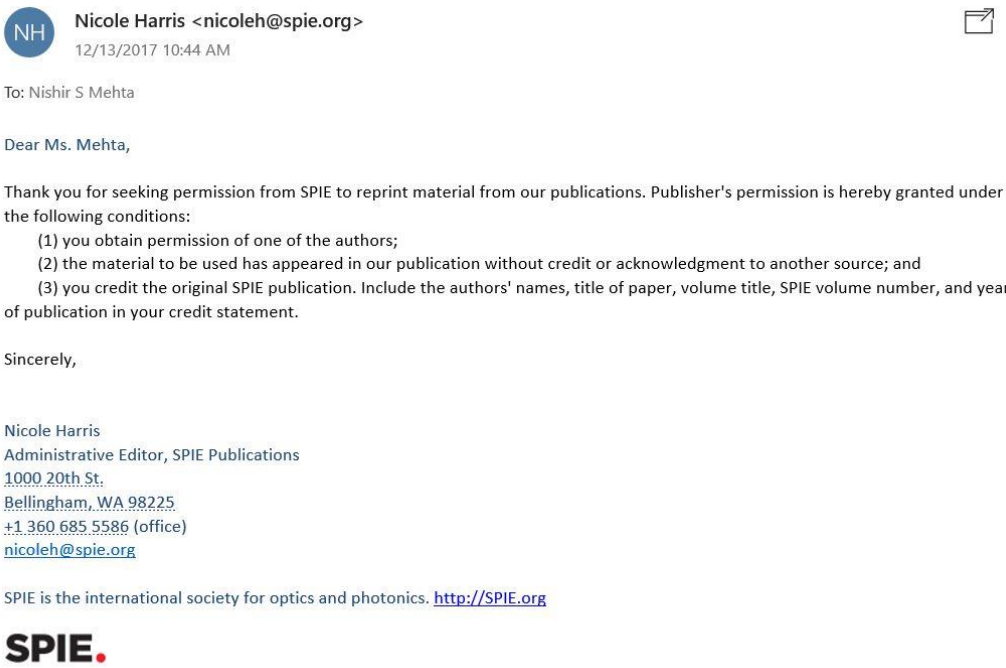

Figure C.3: Permission from SPIE Digital Library

VITA

Nishir Mehta lived in India till August 2015. Nishir was born in the family of engineer father and uncles which instilled passion for science and engineering from his childhood. Nishir received his Bachelor of Technology degree in Mechanical Engineering in 2015 at NMIMS University, Mumbai, India. In order to broaden his horizon and seek research experience, he came to United States of America to pursue graduate education in mechanical engineering. Nishir thoroughly enjoyed working under Dr. Manas Gartia at Applied Nanophotonics Lab. Nishir is passionate about harnessing the power of light to solve problems in the realm of healthcare, energy, and materials. Nishir passed his final MS-thesis defense examination on December 14, 2017 and is a candidate for the Master of Science degree in Mechanical Engineering to be awarded at the December 2018 commencement at Louisiana State University. Nishir is continuing as a PhD researcher with the same group and is excited to face new challenges and opportunities.